In-depth cross-coupling analysis in high-performance induction motor control

Luis A. Amézquita-Brooks[a], Carlos E. Ugalde-Loo[b,*],
Eduardo Licéaga-Castro[a], Jesús Licéaga-Castro[c]

[a] *CIIIA-FIME, Universidad Autónoma de Nuevo León, Monterrey, Km 2.3 Carr. a Salinas Victoria, Apodaca, Nuevo León, C.P. 66600, México*
[b] *School of Engineering, Cardiff University, Queen's Buildings, The Parade, Cardiff, Wales, CF24 3AA, UK*
[c] *Depto. de Electrónica, UAM-Azcapotzalco, D.F., Avenida San Pablo 180, Azcapotzalco, Reynosa Tamaulipas, Ciudad de México, D.F., 02200, México*

Abstract

High-performance field oriented control (FOC) of induction motors (IMs) relies on the accurate control of their electrical dynamics. In particular, perfect decoupling control of the stator currents should be ideally achieved for a FOC scheme to be efficient. However, the decoupling effectiveness afforded by most stator currents controllers may be influenced not only by the parameters and the operating condition, but also by the specific controller structure and the adopted coordinate system. A measure to assess decoupling effectiveness is non-existent in the IM control literature. To bridge this gap, an in-depth analysis of the cross-coupling inherent characteristics of the electrical subsystem of IMs under different well-known control structures is presented in this paper. Specifically, four control strategies previously studied and experimentally validated in the literature are critically assessed in this work: (1) stationary frame proportional-integral (PI) control, (2) synchronous frame PI control, (3) synchronous frame PI control with decoupling networks, and (4) improved stationary frame diagonal control. The decoupling capabilities of controllers in stationary and synchronous coordinates are examined, with a detailed insight on the role of decoupling methods. The analysis is performed in the frequency domain under the framework of individual channel analysis and design (ICAD). By application of ICAD, the decoupling effectiveness of FOC schemes is clearly exposed and quantified, with an assessment of the effects of parametric uncertainty being carried out for completeness. The effect of the inverter dynamics over cross-coupling is also treated using digital simulations. The results are useful to determine the conditions in which each control strategy has either advantages or disadvantages. Additionally, it is

---

* Corresponding author.
  E-mail address: Ugalde-LooC@cardiff.ac.uk (C.E. Ugalde-Loo).

possible to determine the effect of several operating parameters over the stator currents cross-coupling such as nominal flux and torque levels.

1. Introduction

Induction motors (IMs) are the most commonly used high-power electric machines in several industrial applications. Originally IMs were employed in open-loop setups with limited energy efficiency. Further developments made possible a widespread adoption of closed-loop control, resulting in high-performance schemes with higher efficiency [1–3].

Field oriented control (FOC), also known as vector control, is a commonly adopted scheme for IM control [4–7]. Under ideal conditions, IMs employing rotor flux FOC schemes behave like dc motors. Conversely, stator flux FOC allows induction generators (IGs) to behave like dc generators. The approach enables stator or rotor voltages to be excited in such a way that the stator or rotor currents are decoupled. This produces flux- and torque-generating currents analogue to those of a dc machine [6,7]. In addition to a better transient performance, decoupling of currents allows IMs to be driven more efficiently.

The most popular FOC schemes for the stator currents are based on proportional-integral (PI) controllers [8–10], although significant effort has also been dedicated to non-linear decoupling schemes [11–18]. For low-performance applications a pair of stationary reference frame PIs is sufficient to comply with the required specifications, although a high-performance is also possible by introducing slightly more complex control structures [19]. The possibility of affording effective stator currents control that relies on simple PI structures as a baseline is due to the inherent structural robustness characteristics of the IM, as explained in detail in [20]. However, it is commonly accepted that a much higher performance may be attained through the use of controllers in a synchronous frame in addition to decoupling networks [9,21,22]. Such networks aim at decoupling the stator currents by introducing feed-forward terms that compensate the back electro-motive-force (emf) [8–10,23]. All of these control schemes have the ultimate objective of further reducing the cross-coupling of the stator current subsystem.

The electric subsystem of an IM is normally represented by a nonlinear fourth order multiple-input multiple-output (multivariable, MIMO) system [1–3]. It is common practice to simplify this model for control design, with simplifications going as far as using first order monovariable approximations with a time delay [1–5,8–10,19,24]. Although this approach has been successful, it could be argued that the control design is further influenced by the model [8,19]. Moreover, a fundamental limitation exists when neglecting or canceling the multivariable nature of the process, as it is not possible to assess the effect of detuned decoupling networks due to parametric variations. The interested reader is referred to [25], where a detailed analysis on the shortcomings resulting from model over-simplifications is reported. Similarly, it is not possible to compute the actual cross-coupling of the system to formally address the effectiveness of the decoupling scheme. Therefore, a theoretical study employing a unified measurement convention that allows comparing the resulting decoupling

of the most popular stator currents control schemes without model over-simplification is currently missing in the literature.

It has been experimentally shown in [8,19] that different stator currents control schemes are capable of achieving the same level of performance regardless of the reference frame being employed. Assuming that such an observation is true, it could be argued that the simplest control scheme would be the best for a given bandwidth specification. However, to the best knowledge of the authors, a formal theoretical justification or a means to measure the decoupling performance of synchronous and stationary frame schemes is unavailable in the literature. Another recent reference addresses the design of synchronous frame PI controllers for the stator currents with the specific purpose of cross-coupling reduction [26]. As in [8], it is experimentally confirmed that a higher gain, and thus bandwidth, results in an improved decoupling performance. The main shortcoming of these references is the absence of a theoretical framework to study the decoupling properties of the presented control schemes—irrespectively of the selected reference frame.

Individual channel analysis and design (ICAD) is a control framework that has been used to analyze and measure the cross-coupling of MIMO systems [27]. ICAD allows a formal evaluation of system performance, robustness and cross-coupling regardless of the control approach and the controller structure. A distinctive feature of ICAD is the possibility to state the results using well-known engineering concepts in the frequency domain. Bearing in mind these characteristics, a theoretical framework based on ICAD for analyzing, measuring and comparing the decoupling performance achieved by the most common stator currents schemes is presented. The following schemes are assessed: stationary frame PI control, stationary frame diagonal control (non-PI), synchronous frame PI control, and synchronous frame PI control with decoupling networks. The effects of parametric perturbations and bandwidth over the cross-coupling and performance are investigated. Full IM models are employed to incorporate operating conditions into the study (*e.g.*, nominal flux and torque levels). In order to support the theoretical findings and to investigate the influence of the inverter dynamics over the cross-coupling of the electrical subsystem, a set of digital simulations is presented. This is accompanied by a statistical analysis of the time-domain results to provide a quantitative complement to the simulations.

Although the relative gain array (RGA) is a MIMO control tool commonly employed to evaluate the cross-coupling of input-output pairings at steady-state [28,29], it does not play any role in the design stage of a controller. Hence, it cannot be employed to assess the decoupling afforded by a control system and, therefore, its use is avoided in this work. Conversely, the framework afforded by ICAD goes beyond the RGA matrix analysis as it not only enables an evaluation of the decoupling performance of a control system design, but it also allows to address the effect of specific control structures and the robustness of the system. Detailed discussion on the characteristics and limitations of the RGA matrix and a direct comparison with tools from the ICAD framework are provided in [30,31].

It should be highlighted that this work is focused on IMs; however, the analysis and approach here presented are equally valid for IGs. Additionally, this work does not attempt to recommend the adoption of stationary frame stator current controllers over their synchronous frame counterparts (or viceversa). Instead, a methodology to quantify the internal coupling using either approach is presented; this way the control system designer can make an informed decision on which alternative to employ according to their needs to achieve the application requirements.

It must be emphasized that all control schemes studied in this work have been reported and experimentally validated in published references. In particular, stationary and synchronous frame PI schemes with and without decoupling structures are well-known and experimental results are widespread; for instance, the reader is referred to [5,8,19,26]. In this context, the main objective of this paper is neither to propose a novel control scheme nor to experimentally validate a specific controller, but to instead provide a theoretical framework which allows comparing the decoupling properties of different control strategies in stationary or synchronous reference frames. As a result, experimental work is out of the scope of this paper.

2. IM models

An accurate quantification of cross-coupling and perturbation effects cannot be assessed with simplified models of the IM which omit inherent dynamic characteristics. Therefore, the first step for studying these phenomena consists in selecting a model that does not hide the coupled nature of the subsystem. The models adopted in this paper (and included in this section for completeness) fully account the multivariable nature of the IM, capture the effect of the rotor angular speed, and consider the electrical characteristics of the rotor.

2.1. Stationary coordinates model

For a stationary reference frame, the IM model containing the most relevant dynamics is given by [1–3]:

$$
\begin{aligned}
\dot{i}_{\alpha s} &= -a_{11}i_{\alpha s} + a_{13}\psi_{\alpha r} + a_{14}\omega_r\psi_{\beta r} + b_{11}\upsilon_{\alpha s}, \\
\dot{i}_{\beta s} &= -a_{11}i_{\beta s} - a_{14}\omega_r\psi_{\alpha r} + a_{13}\psi_{\beta r} + b_{11}\upsilon_{\beta s}, \\
\dot{\psi}_{\alpha r} &= a_{42}i_{\alpha s} - a_{44}\psi_{\alpha r} - \omega_r\psi_{\beta r}, \\
\dot{\psi}_{\beta r} &= a_{42}i_{\beta s} + \omega_r\psi_{\alpha r} - a_{44}\psi_{\beta r},
\end{aligned}
\tag{1}
$$

$$
\begin{aligned}
\tau_E &= K_T\left(\psi_{\alpha r}i_{\beta s} - \psi_{\beta r}i_{\alpha s}\right), \\
\dot{\omega}_r &= \frac{P}{2J}(\tau_E - \tau_L),
\end{aligned}
\tag{2}
$$

with

$$
a_{11} = \frac{L_r^2 R_s + L_m^2 R_r}{\sigma L_s L_r^2}, \quad a_{13} = \frac{L_m R_r}{\sigma L_s L_r^2}, \quad a_{14} = \frac{L_m}{\sigma L_s L_r},
$$

$$
a_{42} = \frac{L_m R_r}{L_r}, \quad a_{44} = \frac{R_r}{L_r}, \quad b_{11} = \frac{1}{\sigma L_s},
$$

$$
\sigma = 1 - \frac{L_m^2}{L_s L_r}, \quad K_T = \frac{3}{2}\left(\frac{P}{2}\right)\frac{L_m}{L_r},
\tag{3}
$$

where $i_{\alpha s}$ and $i_{\beta s}$ are the stator currents; $\psi_{\alpha r}$ and $\psi_{\beta r}$ the rotor fluxes; ω_r the rotor angular velocity (electrical); $\upsilon_{\alpha s}$ and $\upsilon_{\beta s}$ the stator voltages; L_s, L_r and L_m the stator, rotor and mutual inductances; R_s and R_r the stator and rotor resistances; J the rotor inertia; τ_L the external torque load; τ_E the generated torque; K_T the torque constant; P the number of poles; and σ the dispersion coefficient.

In most IM applications the rotor angular speed ω_r operates at a bandwidth much smaller than that of the electrical subsystem. In particular, a bandwidth separation of two orders (*e.g.*, 40 rad/s versus 4000 rad/s) is typical. This allows considering ω_r as a constant in some situations. In this case system (1)–(2) can be approximated accurately with the first four differential equations in (1), which then become a *linear time invariant* (LTI) system. This system can be used to assess the cross-coupling of the stationary stator currents.

2.2. Synchronous coordinates model

An evaluation of the coupling in synchronous schemes is only possible with a model which contains all the relevant dynamics of system (1) in synchronous coordinates. An equivalent model expressed in coordinates at an arbitrary angular speed ω_e can be obtained by defining the following rotations:

$$
\begin{bmatrix} i_{ds} \\ i_{qs} \end{bmatrix} \triangleq e^{\Gamma\phi_e} \begin{bmatrix} i_{\alpha s} \\ i_{\beta s} \end{bmatrix}, \quad \begin{bmatrix} \psi_{dr} \\ \psi_{qr} \end{bmatrix} \triangleq e^{\Gamma\phi_e} \begin{bmatrix} \psi_{\alpha r} \\ \psi_{\beta r} \end{bmatrix}, \quad \begin{bmatrix} \upsilon_{ds} \\ \upsilon_{qs} \end{bmatrix} \triangleq e^{\Gamma\phi_e} \begin{bmatrix} \upsilon_{\alpha s} \\ \upsilon_{\beta s} \end{bmatrix}, \tag{4}
$$

where the rotation matrix $e^{\Gamma\phi_e}$ is defined as

$$
e^{\Gamma\phi_e} = \begin{bmatrix} \cos\phi_e & \sin\phi_e \\ -\sin\phi_e & \cos\phi_e \end{bmatrix}, \tag{5}
$$

with

$$
\Gamma = \begin{bmatrix} 0 & 1 \\ -1 & 0 \end{bmatrix}, \quad \phi_e = \int \omega_e dt.
$$

In this manner i_{ds} and i_{qs} are the rotated stator currents; ψ_{dr} and ψ_{qr} the rotated rotor fluxes; and υ_{ds} and υ_{qs} the rotated stator voltages. By noting that

$$
\begin{bmatrix} \dot{x}_{\alpha s} \\ \dot{x}_{\beta s} \end{bmatrix} = \frac{d\left(e^{-\Gamma\phi_e} \begin{bmatrix} x_{ds} \\ x_{qs} \end{bmatrix} \right)}{dt} = \begin{bmatrix} \dot{x}_{ds} \\ \dot{x}_{qs} \end{bmatrix} - e^{-\Gamma\phi_e} \Gamma\omega_e \begin{bmatrix} x_{ds} \\ x_{qs} \end{bmatrix},
$$

and by introducing the slip ϕ:

$$
\omega_e \triangleq \omega_r + \phi, \tag{6}
$$

it is possible to rewrite system (1) as:

$$
\begin{aligned}
\dot{i}_{ds} &= -a_{11}i_{ds} + (\omega_r + \phi)i_{qs} + a_{13}\psi_{dr} + a_{14}\omega_r\psi_{qr} + b_{11}\upsilon_{ds}, \\
\dot{i}_{qs} &= -(\omega_r + \phi)i_{ds} - a_{11}i_{qs} - a_{14}\omega_r\psi_{dr} + a_{13}\psi_{qr} + b_{11}\upsilon_{qs}, \\
\dot{\psi}_{dr} &= a_{42}i_{ds} - a_{44}\psi_{dr} + \phi\psi_{qr}, \\
\dot{\psi}_{qr} &= a_{42}i_{qs} - \phi\psi_{dr} - a_{44}\psi_{qr}.
\end{aligned} \tag{7}
$$

The equations provided in system (7) will be employed to assess the cross-coupling of synchronous stator currents control schemes.

3. A brief overview of ICAD

For completeness and aiming to make of this a standalone article, a brief introduction of ICAD is presented next. The ICAD setup for a 2×2 process is considered as this is consistent with the stationary and synchronous coordinates IM models (1) and (7), respectively, although higher order examples can be found in [32,33]. The reader is encouraged to revise the references presented in this section for a thorough understanding of the framework—which falls beyond the scope of this work.

ICAD is a multivariable analysis and control design framework that may be employed to assess the potential and limitations for feedback control design. Even when it is based on diagonal control structures, it may be applied to any MIMO LTI system regardless of its cross-coupling [27,30]. An advantage of ICAD is the possibility to capture the required design specifications, plant attributes and the multivariable feedback control design task into an interactive process. Let a linear 2×2 plant be represented by

$$\mathbf{y}(s) = \mathbf{G}(s)\mathbf{u}(s),$$
$$\begin{bmatrix} y_1(s) \\ y_2(s) \end{bmatrix} = \begin{bmatrix} g_{11}(s) & g_{12}(s) \\ g_{21}(s) & g_{22}(s) \end{bmatrix} \begin{bmatrix} u_1(s) \\ u_2(s) \end{bmatrix}, \tag{8}$$

where $g_{ij}(s)$ represents scalar individual transfer functions, $y_i(s)$ the outputs, $u_i(s)$ the inputs and $r_i(s)$ the reference signals (with $i, j = 1, 2$). Let a diagonal controller matrix be

$$\mathbf{u}(s) = \mathbf{K}(s)\mathbf{e}(s),$$
$$\begin{bmatrix} u_1(s) \\ u_2(s) \end{bmatrix} = \begin{bmatrix} k_1(s) & 0 \\ 0 & k_2(s) \end{bmatrix} \begin{bmatrix} e_1(s) \\ e_2(s) \end{bmatrix},$$
$$e_i(s) = r_i(s) - y_i(s). \tag{9}$$

System (8)–(9) can be represented without any assumption or loss of multivariable information in terms of *individual channels* $c_i(s)$ relating references $r_i(s)$ with outputs $y_i(s)$ as

$$c_i(s) = \frac{y_i(s)}{e_i(s)} = k_i(s)g_{ii}(s)\big(1 - \gamma(s)h_j(s)\big), \tag{10}$$

with $i \neq j$; $i, j = 1, 2$; where

$$\gamma(s) = \frac{g_{12}(s)g_{21}(s)}{g_{11}(s)g_{22}(s)}, \tag{11}$$

$$h_i(s) = \frac{k_i(s)g_{ii}(s)}{1 + k_i(s)g_{ii}(s)}. \tag{12}$$

Given that Eqs. (10) and (12) are single-input single-output (SISO) relations, a classical analysis can be performed. It is known that sensitivity functions assess the capabilities of a control system to reject noise, perturbations and parametric uncertainty. Thus, by analyzing the frequency properties of the sensitivity and complementary sensitivity functions of transfer functions (10) and (12) it is possible to establish a *sensitivity analysis of the overall MIMO control system*. This way, the control design problem reduces to the design of a SISO controller for each channel. Moreover, it can be shown that the stability of the resulting control system in closed-loop is equivalent to the stability of both individual channels (10) in closed-loop. This enables the possibility of testing the stability and robustness of the complete
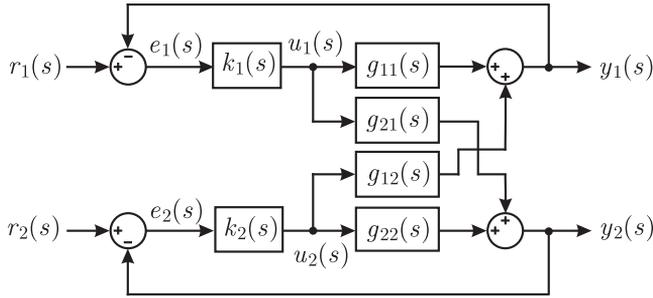
Fig. 1. MIMO 2×2 control system with a diagonal controller.
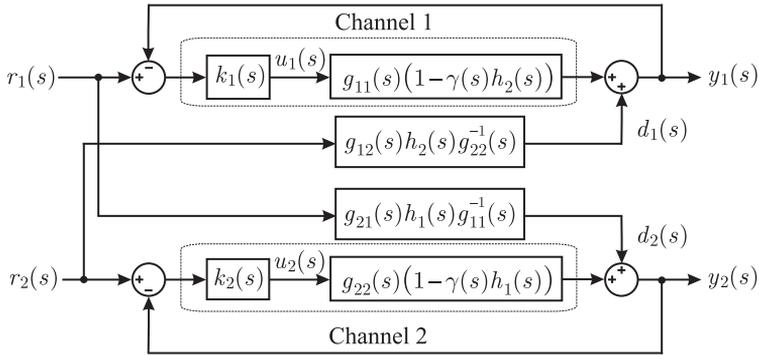
Fig. 2. Equivalent individual channel representation of a 2×2 control system.

MIMO control system with a pair of SISO systems. A block diagram of a feedback system with diagonal control is shown in Fig. 1. The equivalent scalar channels are shown in Fig. 2.

In Eq. (11) $\gamma(s)$ is called *multivariable structure function (MSF)* and it is a fundamental component of ICAD. It is inherent to the nature of the process and reveals important characteristics on the existence of robust controllers satisfying arbitrary specifications. The MSF [19,30]:

- Determines the dynamical characteristics of each input-output configuration.
- Has an interpretation in the frequency domain.
- Its magnitude quantifies the cross-coupling between channels.
- Is related to transmission zeros (zeros of $1 - \gamma(s) = 0 = \det[\mathbf{G}(s)] = g_{11}g_{22} - g_{12}g_{21}$). This allows to test for right hand plane transmission zeros using the Nyquist criterion.
- Its closeness to $(1, 0)$ in the Nyquist plot indicates to what extent the plant zero/pole structure (not necessarily its stability) is sensitive to uncertainty. This fact plays a key role in the design of robust controllers and allows going beyond the concept of bifurcations for non-linear systems.
- Allows a robustness evaluation of decoupling matrices since the zeros of $(1 - \gamma(s))$ are equal to the roots of $\det[\mathbf{G}(s)]$.
- The existence and design of stabilizing diagonal compensators can be determined from the characteristics of $\gamma(s)$. Controllers with a different structure than diagonal can be treated with slight modifications.
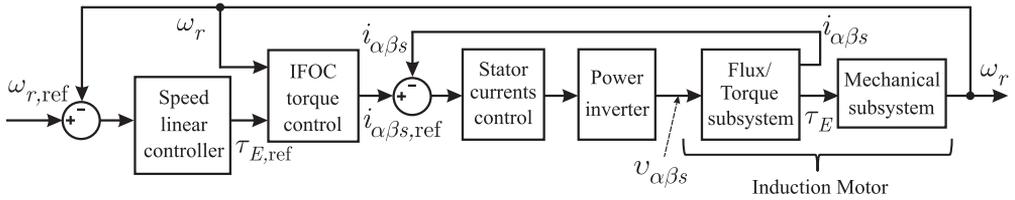
Fig. 3. Block diagram of typical indirect FOC (IFOC) speed scheme.

- Has a close relation with the RGA; however, the RGA is only used to define the selection of input-output pairs as a preliminary step to control design [31].

The MSF expresses the diagonal dominance of multivariable systems in the frequency domain. In this context the magnitude of the MSF is a direct measure of cross-coupling [27,30,31]. A proper interpretation of the MSF allows extending the notions of cross-coupling into the robustness properties of any multivariable system [27] and its quantification is not limited to the maximum peak. The MSF analysis has been used successfully to assess a range of applications and is not limited to IM control (for instance, the reader is directed to [32–40]).

In general, it could be argued that a system with an MSF of high magnitude is more difficult to control with a decentralized controller than one with an MSF of low magnitude [30,41]. This is relevant for the present work since the stator current subsystem is part of an external flux-torque control loop (see Fig. 3).

4. Stationary frame cross-coupling analysis

Let the frequency domain equivalent of system (1) with a constant ω_r be represented by transfer function matrix $\mathbf{G}_{\mathrm{st}}(s)$:

$$\mathbf{y}_{\mathrm{st}}(s) = \mathbf{G}_{\mathrm{st}}(s)\mathbf{u}_{\mathrm{st}}(s),$$

$$\begin{bmatrix} i_{\alpha s}(s) \\ i_{\beta s}(s) \end{bmatrix} = \begin{bmatrix} g_{11,\mathrm{st}}(s) & g_{12,\mathrm{st}}(s) \\ g_{21,\mathrm{st}}(s) & g_{22,\mathrm{st}}(s) \end{bmatrix} \begin{bmatrix} v_{\alpha s}(s) \\ v_{\beta s}(s) \end{bmatrix}. \tag{13}$$

It is possible to design linear diagonal controllers considering input-output individual channels according to Eq. (10) and defined as:

$$c_{1,\mathrm{st}}(s) : v_{\alpha s}(s) \rightarrow i_{\alpha s}(s)$$
$$c_{2,\mathrm{st}}(s) : v_{\beta s}(s) \rightarrow i_{\beta s}(s). \tag{14}$$

That is, the system can be controlled with a diagonal controller

$$\mathbf{u}_{\mathrm{st}}(s) = \mathbf{K}_{\mathrm{st}}(s)\mathbf{e}_{\mathrm{st}}(s),$$

$$\begin{bmatrix} v_{\alpha s}(s) \\ v_{\beta s}(s) \end{bmatrix} = \begin{bmatrix} k_{1,\mathrm{st}}(s) & 0 \\ 0 & k_{2,\mathrm{st}}(s) \end{bmatrix} \begin{bmatrix} e_{\alpha s}(s) \\ e_{\beta s}(s) \end{bmatrix},$$

$$e_{\alpha s}(s) = i_{\alpha s,\mathrm{ref}}(s) - i_{\alpha s}(s), \quad e_{\beta s}(s) = i_{\beta s,\mathrm{ref}}(s) - i_{\beta s}(s). \tag{15}$$

The stator currents control system normally operates within a torque-speed-position FOC loop. The typical stationary frame FOC scheme is depicted in Fig. 3 where $\omega_{r,\mathrm{ref}}$ and $\tau_{E,\mathrm{ref}}$ are the speed and torque references of the FOC control loop.

Let an IM be defined by the parameters provided in Appendix A. The following specifications are considered for the design of stationary frame current controllers:

- A closed-loop bandwidth at a frequency which is a decade higher than the maximum speed (with $\omega_{r,\max} = 376$ rad/s).
- Gain and phase margins over 12 dB and 50°.

Typically, a pair of PI current controllers is designed according to a simplified first order approximation of (13); *i.e.*, $1/(L_s s + R_s)$ [8–10,24]. Better results can be obtained if the full fourth order model is considered (*i.e.,* Model A in [19]). The following PI controllers satisfy the previous specifications:

$$k_{1,\mathrm{st_{PI}}}(s) = k_{2,\mathrm{st_{PI}}}(s) = \frac{566(s + 1000)}{s}. \tag{16}$$

It has been shown in [19] that slightly more complex controller structures can provide better performance than typical PI control. For instance, the following controller, obtained by applying ICAD, also satisfies the aforementioned specifications and improves the performance by increasing the open-loop gain at particular frequencies:

$$k_{1,\mathrm{st_{ICAD}}}(s) = k_{2,\mathrm{st_{ICAD}}}(s) = \frac{566(s + 1000)}{s} \cdot \frac{(s + 400)^2}{s^2 + 100s + 42500} \tag{17}$$

Diagonal controller (17) is essentially a stationary frame PI controller in series with a lag compensator and was designed using Bode shaping techniques (the interested reader is referred to [19] for further details). The performance improvements over the stationary frame PI are due to a high disturbance rejection around $300 - 400$ rad/s, provided by a lag compensator with poles at $-50 \pm j200$ and two zeros at -400. Since the scope of this article is limited to the open and closed-loop cross-coupling evaluation of different control structures and coordinate frames, controller (17) is adopted here for comparison purposes and no further discussion about its design is warranted.

The *open-loop* coupling of system (13) can be assessed through its MSF (11), which yields

$$\gamma_{\mathrm{ol,st}}(s) = \frac{g_{12,\mathrm{st}}(s)g_{21,\mathrm{st}}(s)}{g_{11,\mathrm{st}}(s)g_{22,\mathrm{st}}(s)}. \tag{18}$$

In a similar manner, the closed-loop cross-coupling may be analyzed using an MSF approach. Let the closed-loop control system for (13) with diagonal controller (15) be

$$\mathbf{y}_{\mathrm{st}}(s) = \mathbf{G}_{\mathrm{st}}\mathbf{K}_{\mathrm{st}}(s)\left[\mathbf{I} + \mathbf{G}_{\mathrm{st}}\mathbf{K}_{\mathrm{st}}(s)\right]^{-1}\begin{bmatrix} i_{\alpha s,\mathrm{ref}}(s) \\ i_{\beta s,\mathrm{ref}}(s) \end{bmatrix} = \mathbf{P}_{\mathrm{st}}(s)\mathbf{r}_{\mathrm{st}}(s), \tag{19}$$

where

$$\mathbf{P}_{\mathrm{st}}(s) = \begin{bmatrix} p_{11,\mathrm{st}}(s) & p_{12,\mathrm{st}}(s) \\ p_{21,\mathrm{st}}(s) & p_{22,\mathrm{st}}(s) \end{bmatrix}. \tag{20}$$

The closed-loop MSF of (20) yields:

$$\gamma_{\mathrm{cl,st}}(s) = \frac{p_{12,\mathrm{st}}(s)p_{21,\mathrm{st}}(s)}{p_{11,\mathrm{st}}(s)p_{22,\mathrm{st}}(s)}. \tag{21}$$

Thus, the cross-coupling of system (19) can be quantitatively measured using ICAD's MSF [30,31].
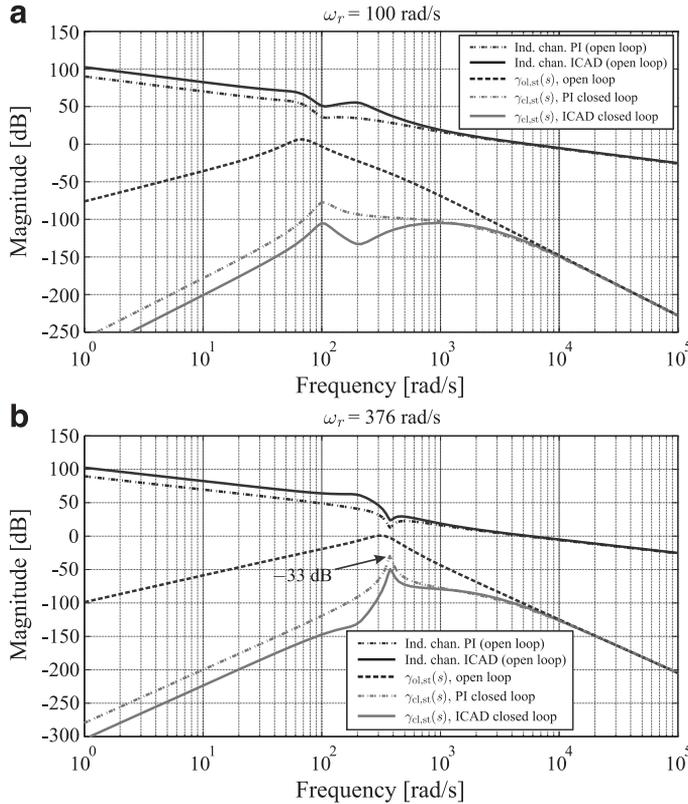
Fig. 4. Open $[\gamma_{ol,st}(s)]$ and closed-loop $[\gamma_{cl,st}(s)]$ cross-coupling comparison for stationary controllers: (a) $\omega_r = 100$ rad/s; (b) $\omega_r = 376$ rad/s.

An attractive aspect of the previous analysis is that it can be used to measure the resulting cross-coupling when using *any* linear stationary frame controller. In this case the typical PI control approach given by Eq. (16) is compared with the diagonal controller (17) designed using ICAD. Fig. 4 shows the Bode plots of $\gamma_{cl,st}(s)$ and $\gamma_{ol,st}(s)$ for the rotor speeds $\omega_r = \{100$ rad/s, 376 rad/s$\}$. *Individual channel* $c_{1,st}(s)$ is also presented in Fig. 4 to gain further insight on how the controller decouples the system. Notice that $c_{1,st}(s)$ is the equivalent *open-loop* frequency response of $p_{11,st}(s)$, since $p_{11,st}(s) = c_{1,st}(s) \cdot (1 + c_{1,st}(s))^{-1}$, with $c_{1,st}(s) = k_{1,st}g_{11,st}(s)\big(1 - \gamma_{ol,st}(s)h_{2,st}(s)\big)$ and $h_{2,st}(s) = k_{2,st}(s)g_{22,st}(s) \cdot (1 + k_{2,st}(s)g_{22,st}(s))^{-1}$.

For both stationary control schemes the following observations apply. It is clear from Fig. 4 that the worst closed-loop cross-coupling (*i.e.,* magnitude of $\gamma_{cl,st}(s)$) occurs at higher rotor speeds ω_r, even when the open-loop cross-coupling $\gamma_{ol,st}(s)$ is similar in both cases of rotor speed. It is interesting to note that if controller $k_{1,st}(s)$ is designed so that a high open-loop individual channel gain is achieved, this ensures that the closed-loop cross-coupling is significantly lower when compared to the cross-coupling in open-loop. Conversely, a low open-loop individual channel gain would yield a closed-loop cross-coupling similar to that in open-loop. Therefore, it can be concluded that a controller offering a high gain tends to reduce the coupling; this is in line with the observed experimental responses using resonant controller elements [8,10]. Fig. 4 also shows that the closed-loop maximum cross-coupling magnitude

lies around the rotor angular velocity. This cross-coupling magnitude is higher when the rotor speed is at its maximum operating value since the controller will tend to achieve a lower open-loop gain around these frequencies (given the proximity to its bandwidth).

According with the previous observations, it is relevant that the stationary frame ICAD controller achieves higher open-loop gain (given by the individual channel) than the stationary frame PI controller. This translates in a reduced closed-loop cross-coupling, which is clearly visible as $\gamma_{\mathrm{cl,st}}(s)$ for the ICAD controller is lower than for the PI.

A stable and minimum phase system is normally easy to control with a decentralized structure if the system has a cross-coupling < -20 dB (10%) as measured by the MSF [27]. A lower cross-coupling (< -40 dB) indicates a highly diagonal dominant system, which is the case for the IM with the stationary ICAD controller (see Fig. 4). This means that the effect of the stator current subsystem cross-coupling over the external flux-torque control loop is negligible. On the other hand, the stationary frame PI controller also achieves a good level of decoupling without reaching the level of a highly diagonal dominant system.

It should be noticed that there may be additional cross-coupling dynamics on the flux-torque subsystem if the IFOC controller is detuned. These are normally related to perturbations of the rotor time constant [1–3,19]. However, a further decrease in the stator currents cross-coupling will bring no additional improvements.

The assessment of the cross-coupling using the MSF provides valuable frequency-related information. For instance, the outer flux-torque control loops can be designed to achieve a high perturbation rejection around troublesome frequencies (*i.e.,* those where the magnitude of the MSF is high) and, as a consequence, to further reduce the effects of the stator currents cross-coupling. It is also worth mentioning that it was possible to improve the decoupling achieved by the stationary frame PI by introducing very simple modifications in the ICAD controller. This further shows that the proposed tool can be useful to compare and improve the decoupling properties of stationary frame control schemes.

5. Synchronous frame cross-coupling analysis

The assessment of cross-coupling in the synchronous frame presents a number of difficulties since a well-known theoretical and analytical framework where high order models comprise the coupling is not existent. It is common to adopt simplified first order SISO models plus a delay [8]. In particular, the assessment of the effect of the system perturbation over the cross-coupling has not been fully studied. To bridge this gap, a theoretical framework for the assessment of cross-coupling under parametric uncertainties in the synchronous frame is developed in this section.

5.1. Synchronous cross-coupling considering FOC

Synchronous frame stator currents controllers for system (7) can be designed according to the following structure:

$$\mathbf{u}_{\mathrm{syn}}(s) = \mathbf{K}_{\mathrm{syn}}(s)\mathbf{e}_{\mathrm{syn}}(s),$$

$$\begin{bmatrix} \upsilon_{ds}(s) \\ \upsilon_{qs}(s) \end{bmatrix} = \begin{bmatrix} k_{1,\mathrm{syn}}(s) & 0 \\ 0 & k_{2,\mathrm{syn}}(s) \end{bmatrix} \begin{bmatrix} e_{ds}(s) \\ e_{qs}(s) \end{bmatrix},$$

$$e_{ds}(s) = i_{ds,\mathrm{ref}}(s) - i_{ds}(s), \quad e_{qs}(s) = i_{qs,\mathrm{ref}}(s) - i_{qs}(s) \tag{22}$$

Typically $k_{1,\text{syn}}(s)$ and $k_{2,\text{syn}}(s)$ are PI controllers. To obtain a quantification of the closed-loop cross-coupling, let the closed-loop control system with (7) and (22) be

$$
\mathbf{y}_{\text{syn}}(s) = \mathbf{P}_{\text{syn}}(s)\mathbf{r}_{\text{syn}}(s),
$$
$$
\begin{bmatrix} i_{ds}(s) \\ i_{qs}(s) \end{bmatrix} = \begin{bmatrix} p_{11,\text{syn}}(s) & p_{12,\text{syn}}(s) \\ p_{21,\text{syn}}(s) & p_{22,\text{syn}}(s) \end{bmatrix} \begin{bmatrix} i_{ds,\text{ref}}(s) \\ i_{qs,\text{ref}}(s) \end{bmatrix}.
\tag{23}
$$

At a first glance it may seem that the closed-loop cross-coupling could be analyzed following a similar approach as in Section 4. However, system (7) contains an additional variable, the slip ϕ, which can be effectively considered as an input [5]. This does not allow a direct calculation of the closed-loop response as it was done for the stationary case.

To fully consider the effect of the slip ϕ it is important to recall that the stator current subsystem is part of an external flux-torque-speed closed-loop scheme (Fig. 3). The typical IFOC controller equations are given by [2,5]

$$
i_{ds,\text{ref}} \triangleq \frac{1}{\overline{L}_m}\psi_{\text{ref}}, \quad i_{qs,\text{ref}} \triangleq \frac{T_{E,\text{ref}}}{\psi_{\text{ref}}\overline{K}_T}, \quad \phi \triangleq \frac{\overline{a}_{42}\overline{R}_r}{\psi_{\text{ref}}}i_{qs,\text{ref}}.
\tag{24}
$$

where ψ_{ref} is the rotor flux reference and the bar $(\overline{\chi})$ indicates an estimation of parameter χ. In general IFOC is devised by selecting appropriate references for the synchronous stator currents. Considering the expressions in (24) it is possible to express the slip as

$$
\phi = \frac{\overline{a}_{44}i_{qs,\text{ref}}}{i_{ds,\text{ref}}}.
\tag{25}
$$

Therefore, the unknown input form system (7) can be eliminated by using Eq. (25). The state-space representation of the PI controllers for i_{ds} and i_{qs} can be obtained by letting

$$
\dot{x}_{c,ids} = e_{ds}, \quad \dot{x}_{c,iqs} = e_{qs},
$$
$$
\upsilon_{ds} = I_{ids}x_{c,ids} + P_{ids}e_{ds}, \quad \upsilon_{qs} = I_{iqs}x_{c,iqs} + P_{iqs}e_{qs},
\tag{26}
$$

where P_{ids}, I_{ids}, P_{iqs}, I_{iqs} are the proportional and integral gains and x_{cids}, x_{ciqs} the states. Considering (25) and (26), system (7) becomes

$$
\dot{x}_{c,ids} = i_{ds,\text{ref}} - i_{ds},
$$
$$
\dot{x}_{c,iqs} = i_{qs,\text{ref}} - i_{qs},
$$
$$
\dot{i}_{ds} = -a_{11}i_{ds} + \left(\omega_r + \frac{\overline{a}_{44}i_{qs,\text{ref}}}{i_{ds,\text{ref}}}\right)i_{qs} + a_{13}\psi_{dr}
$$
$$
\quad\quad + a_{14}\omega_r\psi_{qr} + b_{11}\big[I_{ids}x_{c,ids} + P_{ids}(i_{ds,\text{ref}} - i_{ds})\big],
$$
$$
\dot{i}_{qs} = -\left(\omega_r + \frac{\overline{a}_{44}i_{qs,\text{ref}}}{i_{ds,\text{ref}}}\right)i_{ds} - a_{11}i_{qs} - a_{14}\omega_r\psi_{dr}
$$
$$
\quad\quad + a_{13}\psi_{qr} + b_{11}\big[I_{iqs}x_{c,iqs} + P_{iqs}(i_{qs,\text{ref}} - i_{qs})\big],
$$
$$
\dot{\psi}_{dr} = a_{42}i_{ds} - a_{44}\psi_{dr} + \frac{\overline{a}_{44}i_{qs,\text{ref}}}{i_{ds,\text{ref}}}\psi_{qr},
$$
$$
\dot{\psi}_{qr} = a_{42}i_{qs} - \frac{\overline{a}_{44}i_{qs,\text{ref}}}{i_{ds,\text{ref}}}\psi_{dr} - a_{44}\psi_{qr}.
\tag{27}
$$

System (27) is the closed-loop synchronous stator current subsystem which can be used to calculate system (23); however it is clearly nonlinear. Its linear approximation can be obtained

considering $\bar{a}_{44} = \sigma_r a_{44}$ and $L_m = \sigma_L \bar{L}_m$, where σ_r and σ_L are perturbation factors of the *rotor time constant* ($\tau_r = 1/a_{44} = L_r/R_r$) and of the *mutual inductance* (L_m), respectively. Following a linearization exercise, the state-space representation

$$\dot{\mathbf{x}} = \mathbf{A}_{\text{syn}}\mathbf{x} + \mathbf{B}_{\text{syn}}\mathbf{u},$$
$$\mathbf{y} = \mathbf{C}_{\text{syn}}\mathbf{x}, \tag{28}$$

is obtained, with

$$\mathbf{x} = \begin{bmatrix} i_{ds} & i_{qs} & \psi_{dr} & \psi_{qr} & x_{c,ids} & x_{c,iqs} \end{bmatrix}^T,$$
$$\mathbf{u} = \begin{bmatrix} i_{ds,\text{ref}} & i_{qs,\text{ref}} \end{bmatrix}^T, \quad \mathbf{y} = \begin{bmatrix} i_{ds} & i_{qs} \end{bmatrix}^T, \tag{29}$$

and

$$\mathbf{A}_{\text{syn}} = \begin{bmatrix} a_{11,\text{syn}} & a_{12,\text{syn}} & a_{13} & a_{14}\omega_r & b_{11}I_{ids} & 0 \\ -a_{12,\text{syn}} & a_{22,\text{syn}} & -a_{14}\omega_r & a_{13} & 0 & b_{11}I_{iqs} \\ a_{42} & 0 & -a_{44} & a_{34,\text{syn}} & 0 & 0 \\ 0 & a_{42} & -a_{34,\text{syn}} & -a_{44} & 0 & 0 \\ -1 & 0 & 0 & 0 & 0 & 0 \\ 0 & -1 & 0 & 0 & 0 & 0 \end{bmatrix}$$

$$\mathbf{B}_{\text{syn}} = \begin{bmatrix} b_{11}P_{ids} - \sigma_r a_{44}\beta_2 i_{qs0} & \sigma_r a_{44}\beta_1 i_{qs0} \\ \sigma_r a_{44}\beta_3 & b_{11}P_{iqs} - \sigma_r a_{44}\beta_1 i_{ds0} \\ -\sigma_r a_{44}\beta_2 \psi_{qr0} & \sigma_r a_{44}\beta_1 \psi_{qr0} \\ \sigma_r a_{44}\beta_2 \psi_{dr0} & -\sigma_r a_{44}\beta_1 \psi_{dr0} \\ 1 & 0 \\ 0 & 1 \end{bmatrix},$$

$$\mathbf{C}_{\text{syn}} = \begin{bmatrix} 1 & 0 & 0 & 0 & 0 & 0 \\ 0 & 1 & 0 & 0 & 0 & 0 \end{bmatrix}, \tag{30}$$

where χ_0 denotes the equilibrium point of χ. Constants in matrices $\mathbf{A}_{\text{syn}}$ and $\mathbf{B}_{\text{syn}}$ have been defined in (3) and:

$$a_{11,\text{syn}} = -(b_{11}P_{ids} + a_{11}), \quad a_{22,\text{syn}} = -(b_{11}P_{iqs} + a_{11}),$$
$$a_{12,\text{syn}} = \omega_r + \sigma_r a_{44}\beta_3, \quad a_{34,\text{syn}} = \sigma_r a_{44}\beta_3, \tag{31}$$

with

$$\beta_1 = \frac{1}{i_{dsr0}}, \quad \beta_2 = \frac{i_{qsr0}}{i_{dsr0}^2}, \quad \beta_3 = \frac{i_{qsr0}}{i_{dsr0}}. \tag{32}$$

The notation was simplified to $i_{ds,\text{ref0}} = i_{dsr0}$ and $i_{qs,\text{ref0}} = i_{qsr0}$. Equilibrium points must be obtained to use the linear approximation (28). It can be assumed that synchronous PI controllers achieve zero steady-state error; that is:

$$i_{ds0} = i_{dsr0} = \frac{1}{\bar{L}_m}\psi_{\text{ref}}, \quad i_{qs0} = i_{qsr0} = \frac{T_{E,\text{ref}}}{\psi_{\text{ref}}\overline{K}_T} \tag{33}$$

In practical FOC applications the bandwidths of the flux and the torque reference levels are around the bandwidth of the rotor angular speed. Given that the inner stator currents

subsystem is much faster than the angular speed, the flux and torque reference signals can be considered as a constant for the inner subsystem. Nonetheless, the operating condition is given by the *overall* torque and flux levels. Since these parameters are considered in the present study, it is possible to analyze their effects over the stator current cross-coupling. The rotor flux equilibrium points can be obtained by solving the last two equations of (27) in steady-state. This yields

$$
\begin{aligned}
\psi_{dr0} &= \frac{a_{42}\phi_0 i_{qs0} + a_{44}a_{42}i_{ds0}}{a_{44}^2 + \phi_0^2}, \\
\psi_{qr0} &= \frac{-a_{42}\phi_0 i_{ds0} + a_{44}a_{42}i_{qs0}}{a_{44}^2 + \phi_0^2}.
\end{aligned}
\tag{34}
$$

with $\phi_0 = \bar{a}_{44}i_{qsr0}/i_{dsr0}$. Substituting elements of (33) into (34) gives the following equilibrium points for the rotor fluxes:

$$
\begin{aligned}
\psi_{dr0} &= \frac{\sigma_L\left(\overline{K}_T^2\psi_{\text{ref}}^4 + \sigma_r\overline{L}_m^2 T_{E,\text{ref}}^2\right)}{\overline{K}_T^2\psi_{\text{ref}}^4 + \sigma_r^2\overline{L}_m^2 T_{E,\text{ref}}^2}\psi_{\text{ref}}, \\
\psi_{qr0} &= \frac{\overline{K}_T\psi_{\text{ref}}^3 L_m T_{E,\text{ref}}(1 - \sigma_r)}{\overline{K}_T^2\psi_{\text{ref}}^4 + \sigma_r^2\overline{L}_m^2 T_{E,\text{ref}}^2}.
\end{aligned}
\tag{35}
$$

In the absence of perturbations (*i.e.,* $\sigma_r = 1$ and $\sigma_L = 1$), then $\psi_{dr0} = \psi_{\text{ref}}$ and $\psi_{qr0} = 0$, *which is the ideal rotor flux decoupling of FOC schemes*. However, the presence of perturbations induces flux coupling which further affects the stator currents cross-coupling. This conclusion could only be reached through an analysis approach which not only considers the most important effects of the stator current control systems, but also of the perturbed flux-torque subsystem.

Following the calculation of the equilibrium point given by (33)–(35) it is possible to obtain the closed-loop transfer matrix defined in (23) as $\mathbf{P}_{\text{syn}} = \mathbf{C}_{\text{syn}}(s\mathbf{I} - \mathbf{A}_{\text{syn}})^{-1}\mathbf{B}_{\text{syn}}$. Its MSF is given by

$$
\gamma_{\text{cl,syn}}(s) = \frac{p_{12,\text{syn}}(s)p_{21,\text{syn}}(s)}{p_{11,\text{syn}}(s)p_{22,\text{syn}}(s)}.
\tag{36}
$$

Fig. 5 shows the Bode magnitude plot of $\gamma_{\text{cl,syn}}(s)$ at different rotor speeds for the IM given in Appendix A. The PIs have been designed using the first order SISO approximation of the stator currents dynamics: $b_{11}/(s + a_{11})$. Direct pole placement has been performed, with the closed-loop dynamics set at $s = -a$ and proportional and integral gains given as

$$
P_{ids} = P_{iqs} = \frac{2a - a_{11}}{b_{11}}, \quad I_{ids} = I_{iqs} = \frac{a^2}{b_{11}}.
\tag{37}
$$

For this design, the closed-loop poles were set at $s = -3300$, which resulted in the following PI controller:

$$
k_{1,\text{syn}}(s) = k_{2,\text{syn}}(s) = \frac{641.1(s + 1745)}{s}.
\tag{38}
$$

As shown in Fig. 5, the synchronous PI defined by Eq. (38) is capable of achieving a very high level of decoupling. The resulting closed-loop system has the highest level of coupling when it operates at the maximum rotor angular speed (376 rad/s). In addition,
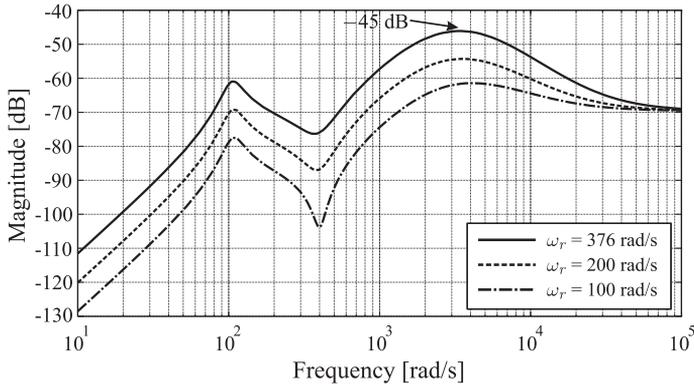
Fig. 5. Closed-loop cross-coupling [$\gamma_{\text{cl,syn}}(s)$] of the synchronous PI controller at different rotor speeds.

when synchronous PI controllers are employed the resulting cross-coupling has mainly two components: at low (≈ 100 rad/s) and at high (≈ 3000 rad/s) frequencies. Due to its magnitude, the most relevant is at the highest frequency.

The open-loop cross-coupling in a synchronous frame cannot be easily calculated due to the presence of slip ϕ in Eq. (7) (only known in closed-loop operation). It could be argued that the isometric transformation given in Eq. (5) preserves the H_2 norm; thus the magnitude of the closed-loop synchronous frame cross-coupling may be compared to the stationary one (Fig. 4). However such a comparison is not direct as the references in each frame are different. A further discussion on this is presented in Section 9 with the aid of digital simulations.

5.2. Synchronous cross-coupling with decoupling networks

The use of decoupling networks has been commonly proposed in the literature with the aim of further reducing the cross-coupling. There are several available configurations for decoupling networks. In this section a generalized network is presented and then an embodiment of this generalization is derived for indirect rotor-flux FOC—which results in the typical back-emf stator decoupling network [8].

To fully decouple the first two equations of system (7) the stator voltages should be given as

$$v_{ds} = \widehat{v}_{ds} - \frac{1}{b_{11}}\big[(\omega_r + \phi)i_{qs} + a_{13}\psi_{dr} + a_{14}\omega_r\psi_{qr}\big],$$

$$v_{qs} = \widehat{v}_{qs} - \frac{1}{b_{11}}\big[-(\omega_r + \phi)i_{ds} - a_{14}\omega_r\psi_{dr} + a_{13}\psi_{qr}\big], \tag{39}$$

where $\widehat{v}_{ds}$ and $\widehat{v}_{qs}$ are the decoupled stator voltages. If the previous condition holds then the stator currents decouple, resulting in

$$\dot{i}_{ds} = -a_{11}i_{ds} + b_{11}\widehat{v}_{ds},$$

$$\dot{i}_{qs} = -a_{11}i_{qs} + b_{11}\widehat{v}_{qs}. \tag{40}$$

As it can be observed, expressions in Eq. (40) represent similar SISO approximations to the one discussed in Section 5.1. Therefore, the design method summarized by (37) may be used and PI controllers defined in Eq. (38) adopted.

The difficulty with the previous approach is that the rotor fluxes ψ_{dr} and ψ_{qr} are not known. A simple alternative is to assume that the rotor flux FOC controller is properly tuned. In this condition, $\psi_{dr} = \psi_{\text{ref}} = \overline{L}_m i_{ds,\text{ref}}$ and $\psi_{qr} = 0$ [from Eq. (33)]. Therefore, the decoupling inputs for Eq. (39) become

$$
\upsilon_{ds} = \widehat{\upsilon}_{ds} - \frac{1}{b_{11}}\big(\omega_r i_{qs} + \phi i_{qs} + \overline{a}_{13}\overline{L}_m i_{ds,\text{ref}}\big),
$$
$$
\upsilon_{qs} = \widehat{\upsilon}_{qs} - \frac{1}{b_{11}}\big(-\omega_r i_{ds} - \phi i_{ds} - \overline{a}_{14}\overline{L}_m \omega_r i_{ds,\text{ref}}\big).
\tag{41}
$$

where the bar $(\overline{\chi})$ indicates an estimation of χ. It is worth recalling that in this paper perturbations on the mutual inductance (L_m) and the rotor time constant ($\tau_r = 1/a_{44} = L_r/R_r$) are considered. In a real IM both the stator and rotor inductances would be also perturbed when the mutual inductance is perturbed. Thus, it is assumed that $L_s = \sigma_L \overline{L}_s$ and $L_r = \sigma_L \overline{L}_r$. Bearing this in mind and according to Eq. (3), then $\overline{a}_{14}\overline{L}_m = a_{14}L_m$ and $\overline{a}_{13}\overline{L}_m = a_{14}L_m \overline{a}_{44}$. Additionally, b_{11} can be measured with a high degree of precision during the identification process documented in [42]; hence it is assumed that $\overline{b}_{11} \approx b_{11}$. Considering the previous discussion and by introducing inputs given in Eq. (41) and the slip of the IFOC controller (25) into system (7), the following system is obtained:

$$
\dot{i}_{ds} = -a_{11}i_{ds} + a_{13}\psi_{dr} + a_{14}\omega_r \psi_{qr} + b_{11}\widehat{\upsilon}_{ds} - a_{14}L_m \overline{a}_{44} i_{ds,\text{ref}},
$$
$$
\dot{i}_{qs} = -a_{11}i_{qs} - a_{14}\omega_r \psi_{dr} + a_{13}\psi_{qr} + b_{11}\widehat{\upsilon}_{qs} + a_{14}\omega_r L_m i_{ds,\text{ref}},
$$
$$
\dot{\psi}_{dr} = a_{42}i_{ds} - a_{44}\psi_{dr} + \frac{\overline{a}_{44}i_{qs,\text{ref}}}{i_{ds,\text{ref}}}\psi_{qr},
$$
$$
\dot{\psi}_{qr} = a_{42}i_{qs} - \frac{\overline{a}_{44}i_{qs,\text{ref}}}{i_{ds,\text{ref}}}\psi_{dr} - a_{44}\psi_{qr}.
\tag{42}
$$

If a synchronous PI controller as in (26) is employed, the closed-loop system results in:

$$
\dot{x}_{c,ids} = i_{ds,\text{ref}} - i_{ds},
$$
$$
\dot{x}_{c,iqs} = i_{qs,\text{ref}} - i_{qs},
$$
$$
\begin{aligned}
\dot{i}_{ds} = &-\big(b_{11}P_{ids} + a_{11}\big)i_{ds} + a_{13}\psi_{dr} + a_{14}\omega_r \psi_{qr}\\
&+b_{11}I_{ids}x_{c,ids} + \big(b_{11}P_{ids} - a_{14}L_m \overline{a}_{44}\big)i_{ds,\text{ref}},
\end{aligned}
$$
$$
\begin{aligned}
\dot{i}_{qs} = &-\big(b_{11}P_{iqs} + a_{11}\big)i_{qs} - a_{14}\omega_r \psi_{dr} + a_{13}\psi_{qr}\\
&+b_{11}I_{iqs}x_{c,iqs} + \big(b_{11}P_{iqs} + a_{14}\omega_r L_m\big)i_{ds,\text{ref}},
\end{aligned}
$$
$$
\dot{\psi}_{dr} = a_{42}i_{ds} - a_{44}\psi_{dr} + \frac{\overline{a}_{44}i_{qs,\text{ref}}}{i_{ds,\text{ref}}}\psi_{qr},
$$
$$
\dot{\psi}_{qr} = a_{42}i_{qs} - \frac{\overline{a}_{44}i_{qs,\text{ref}}}{i_{ds,\text{ref}}}\psi_{dr} - a_{44}\psi_{qr}.
\tag{43}
$$

The closed-loop cross-coupling can be analyzed by calculating the MSF of the linear approximation of system (43) in a similar manner to that presented for the synchronous PI in Section 5.1. The following state-space representation is obtained:

$$
\dot{\mathbf{x}} = \mathbf{A}_{\text{dec}}\mathbf{x} + \mathbf{B}_{\text{dec}}\mathbf{u},
$$
$$
\mathbf{y} = \mathbf{C}_{\text{dec}}\mathbf{x},
\tag{44}
$$

with state, input and output vectors defined as in Eq. (29) and

$$
\mathbf{A}_{\text{dec}} = \begin{bmatrix}
a_{11,\text{syn}} & 0 & a_{13} & a_{14}\omega_r & b_{11}I_{ids} & 0 \\
0 & a_{22,\text{syn}} & -a_{14}\omega_r & a_{13} & 0 & b_{11}I_{iqs} \\
a_{42} & 0 & -a_{44} & a_{34,\text{syn}} & 0 & 0 \\
0 & a_{42} & -a_{34,\text{syn}} & -a_{44} & 0 & 0 \\
-1 & 0 & 0 & 0 & 0 & 0 \\
0 & -1 & 0 & 0 & 0 & 0
\end{bmatrix}
$$

$$
\mathbf{B}_{\text{dec}} = \begin{bmatrix}
b_{11}P_{ids} - a_{14}L_m\sigma_r a_{44} & 0 \\
0 & b_{11}P_{iqs} + a_{14}\omega_r L_m \\
-\sigma_r a_{44}\beta_2\psi_{qr0} & \sigma_r a_{44}\beta_1\psi_{qr0} \\
\sigma_r a_{44}\beta_2\psi_{dr0} & -\sigma_r a_{44}\beta_1\psi_{dr0} \\
1 & 0 \\
0 & 1
\end{bmatrix},
$$

$$
\mathbf{C}_{\text{dec}} = \mathbf{C}_{\text{syn}} \tag{45}
$$

Constants in $\mathbf{A}_{\text{dec}}$ and $\mathbf{B}_{\text{dec}}$ are defined in (3), (31) and (32). The equilibrium point of (43) can be calculated under the same considerations as those for (27). The equilibrium points for both configurations coincide and are defined by (33)–(35).

The closed-loop transfer matrix of the stator currents subsystem considering synchronous PI control and stator decoupling networks is obtained as $\mathbf{P}_{\text{dec}} = \mathbf{C}_{\text{dec}}(s\mathbf{I} - \mathbf{A}_{\text{dec}})^{-1}\mathbf{B}_{\text{dec}}$. The corresponding MSF is given by

$$
\gamma_{\text{cl,dec}}(s) = \frac{p_{12,\text{dec}}(s)p_{21,\text{dec}}(s)}{p_{11,\text{dec}}(s)p_{22,\text{dec}}(s)}, \tag{46}
$$

where:

$$
\mathbf{y}_{\text{dec}}(s) = \mathbf{P}_{\text{dec}}(s)\mathbf{r}_{\text{dec}}(s),
$$
$$
\begin{bmatrix} i_{ds}(s) \\ i_{qs}(s) \end{bmatrix} = \begin{bmatrix} p_{11,\text{dec}}(s) & p_{12,\text{dec}}(s) \\ p_{21,\text{dec}}(s) & p_{22,\text{dec}}(s) \end{bmatrix} \begin{bmatrix} i_{ds,\text{ref}}(s) \\ i_{qs,\text{ref}}(s) \end{bmatrix}. \tag{47}
$$

Fig. 6 shows the Bode magnitude plot of $\gamma_{\text{cl,dec}}(s)$ at different rotor speeds for an IM with parameters described in Appendix A. The PI controllers have been designed according to (37) with $a = 3300$, yielding (38). It can be observed that the resulting cross-coupling when decoupling networks are used together with synchronous PI controller (38) is lower when compared with stationary controller (17) or synchronous PI controller (38) on its own (Figs. 4 and 5). An interesting effect of the decoupling networks is that they also reduce the second high-gain high-frequency peak appearing when only the synchronous PI is used (Fig. 5).

6. Robustness of decoupling schemes: effect of parametric perturbations

Although the use of synchronous PI controllers with decoupling networks decreases cross-coupling by a significant level when compared to stationary controllers, it should be recalled that synchronous schemes are highly dependent on an adequate tuning of the FOC flux-torque controller. It is well-known that FOC schemes are in turn heavily dependent on the knowledge of the rotor time constant, which can be easily perturbed [1–3,5]. In addition,
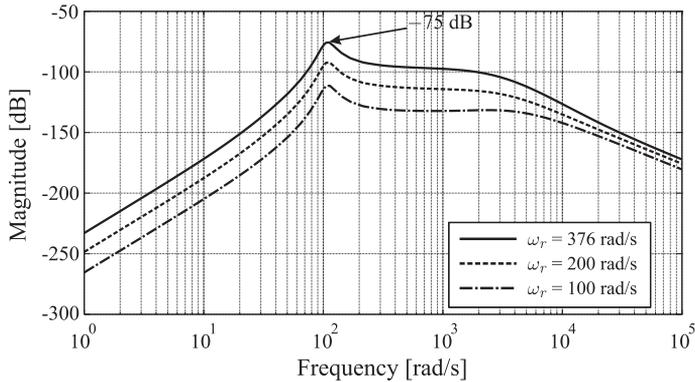
Fig. 6. Closed-loop cross-coupling [$\gamma_{cl,dec}(s)$] of the synchronous PI controller with decoupling networks at different rotor speeds.
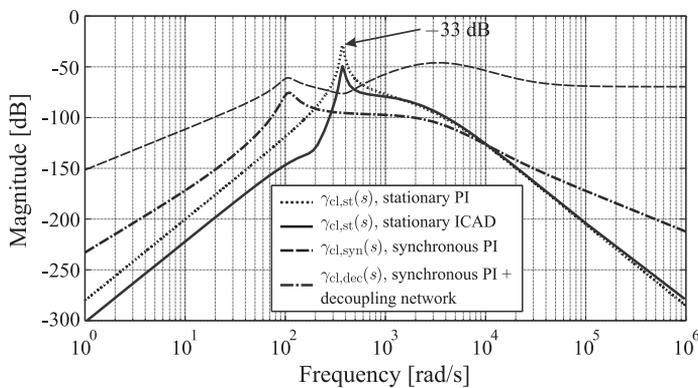
Fig. 7. Unperturbed closed-loop cross-coupling comparison.

the use of decoupling networks further increases such dependency by attempting a direct cancelation of the back-emf. In contrast, a stationary frame controller is independent of these parameters. To address the robustness of the control schemes, the effects of perturbations on the rotor time constant ($\tau_r = 1/a_{44} = L_r/R_r$) and the mutual inductance (L_m) are presented in this section. These perturbations can be easily introduced to the models from Sections 4–5.

Fig. 7 presents the closed-loop cross-coupling under no perturbations as a benchmark for comparison. Since the highest level of cross-coupling occurs at high rotor speeds, all assessments in this section are performed considering the maximum rotor angular speed ($\omega_r = 376$ rad/s for the IM in this work). It is clear that without perturbations the use of synchronous control with decoupling networks offers the best cross-coupling reduction. It should be highlighted though that all schemes achieve a maximum cross-coupling which is lower than -40 dB, except for the stationary frame PI which achieves -33 dB. This is important as such a level is sufficiently low for allowing the design of outer-loop decentralized controllers in other applications [39].

Fig. 8 presents the resulting closed-loop cross-coupling when a slight and a moderate level of perturbations to the rotor time constant are introduced. As it can be seen, these
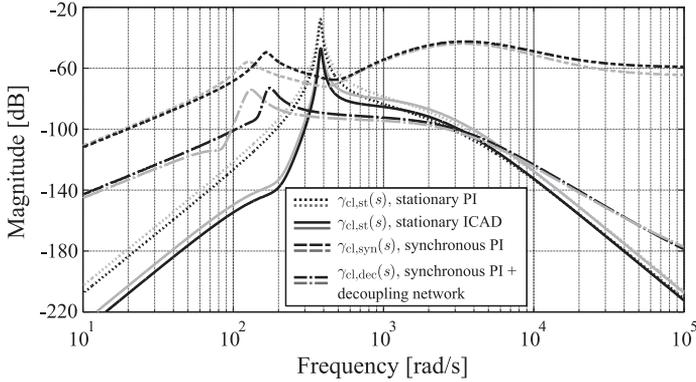
Fig. 8. Closed-loop cross-coupling comparison with perturbations to the rotor time constant: $\sigma_r = 1.6$ (black) and $\sigma_r = 1.2$ (gray).
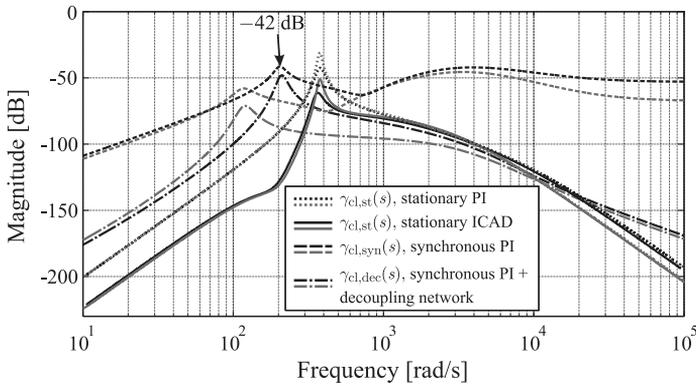
Fig. 9. Closed-loop cross-coupling comparison with perturbations to the mutual inductance: $\sigma_L = 0.5$ (black) and $\sigma_L = 0.9$ (gray).

perturbations have a negative effect for all control strategies, with cross-coupling being increased. It is notable that the stationary controllers render the least affected schemes; however, all strategies retain a similar overall cross-coupling level as in the unperturbed case.

Fig. 9 illustrates the resulting closed-loop cross-coupling upon perturbations to the mutual inductance nominal value. It can be seen that these perturbations have an important negative effect when a synchronous PI controller is employed with decoupling networks. Interestingly enough, cross-coupling is actually reduced for all stationary frame controllers. This effect is due to an increment of the open-loop gain of the system in this condition. However, all strategies achieve a low level of cross-coupling below −40 dB (including the stationary frame PI).

Moderate perturbations to the rotor time constant and to the mutual inductance ($\sigma_r = 1.6$ and $\sigma_L = 0.5$) are shown in Fig. 10. The plots illustrate that the joint effect of these perturbations over synchronous schemes results on a significant increment of the cross-coupling level. The synchronous PI is particularly affected. Conversely the stationary frame controllers and the synchronous PI with decoupling networks maintain a lower level of cross-coupling.

Table 1 summarizes relevant information from Figs. 7–10. The results suggest that the synchronous PI controller on its own has the lowest robustness for certain combinations of
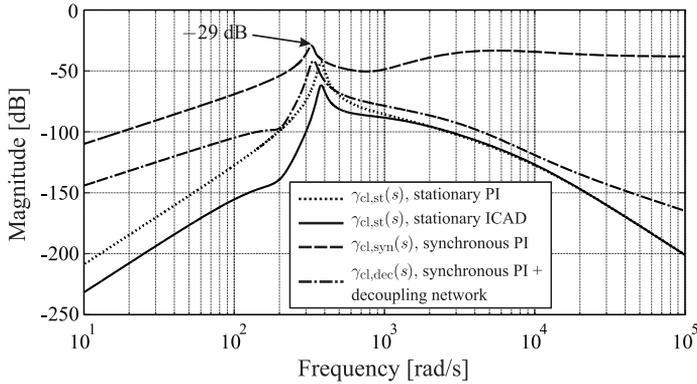
Fig. 10. Closed-loop cross-coupling comparison with perturbations to the rotor time constant and mutual inductance: $\sigma_r = 1.6$ and $\sigma_L = 0.5$.

Table 1
Maximum cross-coupling magnitude ($\omega_r = 376$ rad/s).

Perturbation type	Stationary Frame PI	Stationary Frame ICAD	Synchronous Frame PI	Sync. PI + decoupling
No perturbation	−33 dB	−49 dB	−46 dB	−75 dB
Rotor time constant	−29 dB	−49 dB	−43 dB	−74 dB
Mutual inductance	−43 dB	−61 dB	−42 dB	−48 dB
Both perturbations	−41 dB	−61 dB	−29 dB	−41 dB

perturbations. The addition of decoupling networks provides an enhancement and greatly increases robustness. However, it can be noticed that in the worst case the synchronous PI has a maximum cross-coupling which is sufficiently low: −29 dB.

Regardless of the scheme to be employed for stator currents control, it would be advisable to design the outer flux-torque loop with a bandwidth which avoids the highest level of cross-coupling. For instance, if a stationary frame current controller is desired, Figs. 7 –10 suggest that the flux-torque loop would be less effective due to stator currents cross-coupling if a bandwidth around $300 - 400$ rad/s is employed. As it has been shown in this section, such a quantified measure of cross-coupling is readily available using the MSF analysis under the ICAD framework.

7. Noise and perturbation rejection

In addition to parametric perturbations, the stator currents subsystem is also subject to external disturbances and noise. The most relevant source of external disturbances is the power inverter, which introduces distortion due to the modulation and variations of the dc voltage bus. On the other hand, one of the main sources of noise arises from sensor measurement, which also has a negative effect on the stator currents control subsystem. To complement the results presented in Section 6, the effects of external perturbations in the stator voltages and of sensor measurement noise are studied in this section.

For the control schemes in stationary reference frame, perturbations to stator voltages and sensor noise can be introduced by amending Eq. (9) as follows:

$$
\begin{bmatrix} v_{\alpha s}(s) \\ v_{\beta s}(s) \end{bmatrix} = \begin{bmatrix} k_{1,\mathrm{st}}(s) & 0 \\ 0 & k_{2,\mathrm{st}}(s) \end{bmatrix} \begin{bmatrix} e_{\alpha s}(s) \\ e_{\beta s}(s) \end{bmatrix} + \begin{bmatrix} \delta v_{\alpha s}(s) \\ \delta v_{\beta s}(s) \end{bmatrix},
$$
$$
e_{\alpha s}(s) = i_{\alpha s,\mathrm{ref}}(s) - [i_{\alpha s}(s) + \delta i_{\alpha s}(s)],
$$
$$
e_{\beta s}(s) = i_{\beta s,\mathrm{ref}}(s) - [i_{\beta s}(s) + \delta i_{\beta s}(s)],
\tag{48}
$$

where $\delta v_{\alpha s}$ and $\delta v_{\beta s}$ are the perturbation signals of the stator voltages, and $\delta i_{\alpha s}$ and $\delta i_{\beta s}$ represent sensor noise.

According to Fig. 2, the effects of the stator voltage perturbations over the main outputs is given by

$$
\frac{i_{\alpha s}(s)}{\delta v_{\alpha s}(s)} = \frac{c_{1,\mathrm{st}}(s)}{k_{1,\mathrm{st}}(s)} \cdot \frac{1}{1 + c_{1,\mathrm{st}}(s)}, \quad \frac{i_{\beta s}(s)}{\delta v_{\beta s}(s)} = \frac{c_{2,\mathrm{st}}(s)}{k_{2,\mathrm{st}}(s)} \cdot \frac{1}{1 + c_{2,\mathrm{st}}(s)}.
\tag{49}
$$

Conversely, the effect of sensor noise over the main outputs is provided by

$$
\frac{i_{\alpha s}(s)}{\delta i_{\alpha s}(s)} = \frac{-c_{1,\mathrm{st}}(s)}{1 + c_{1,\mathrm{st}}(s)}, \quad \frac{i_{\beta s}(s)}{\delta i_{\beta s}(s)} = \frac{-c_{2,\mathrm{st}}(s)}{1 + c_{2,\mathrm{st}}(s)}.
\tag{50}
$$

Eqs. (49) and (50) show that the definition of the individual channels used in ICAD as given by (10) allows using the typical *sensitivity* and *complementary sensitivity* equations to assess the effect of input perturbations and sensor noise. These equations apply for both the stationary PI and the ICAD controller.

In the case of the synchronous frame PI control scheme perturbations to the stator voltages and sensor noise can be introduced by amending system (28) as follows:

$$
\dot{\mathbf{x}} = \mathbf{A}_{\mathrm{syn}}\mathbf{x} + \mathbf{B}_{\mathrm{syn}}\mathbf{u} + \mathbf{B}_{\mathrm{syn},\delta}\delta\mathbf{u},
$$
$$
\delta\mathbf{u} = \begin{bmatrix} \delta v_{ds} & \delta v_{qs} \end{bmatrix}^T, \quad \mathbf{u} = \begin{bmatrix} i_{ds,\mathrm{ref}} - \delta i_{ds} & i_{qs,\mathrm{ref}} - \delta i_{qs} \end{bmatrix}^T
\tag{51}
$$

where

$$
\mathbf{B}_{\mathrm{syn},\delta} = \begin{bmatrix} b_{11} & 0 & 0 & 0 & 0 & 0 \\ 0 & b_{11} & 0 & 0 & 0 & 0 \end{bmatrix}^T
\tag{52}
$$

A similar treatment can be used for the synchronous PI scheme with decoupling networks.

Using the aforementioned approach, the response of the system to arbitrary perturbation signals in the stator voltages (*i.e.*, $\delta v_{\alpha s}$, $\delta v_{\beta s}$, δv_{ds} and δv_{qs}) and in the sensor currents (*i.e.*, $\delta i_{\alpha s}$, $\delta i_{\beta s}$, δi_{ds} and δi_{qs}) can be calculated both in the time-domain using simulations and in the frequency domain using Bode plots. Fig. 11 presents the responses of the stator currents error in the frequency domain for all control schemes due to perturbations to the stator voltages and sensor noise when no parametric perturbation is considered. Similarly, Fig. 12 shows the corresponding responses if parametric perturbations ($\sigma_L = 0.5$ and $\sigma_r = 1.6$) are considered.

These Bode plots can be interpreted as the resulting spectrum of the error signals due to normalized random perturbation signals (*i.e.,* white noise). That is, if the perturbation and noise signals had a uniform frequency distribution, the resulting magnitude spectrum of the error induced by the perturbations and noise would be as shown in Fig. 11. This allows for a very general assessment of the perturbation rejection characteristics of control systems because if a more specific perturbation signal is desired then its magnitude spectrum can be
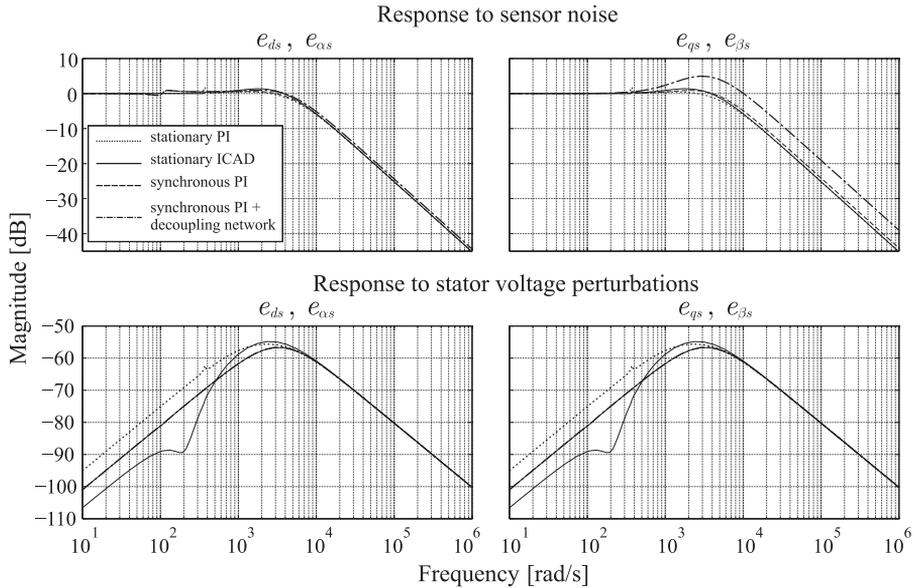
Fig. 11. System response due to perturbations in the stator voltages and sensor noise.

used as a weighting factor (additive) to that presented in Fig. 11. In [43] it was shown that the noise and perturbation rejection of the torque-flux subsystem of IMs can be appropriately characterized using this approach, even after considering system non-linearities.

In this context, sensor noise normally introduces high frequency noise; therefore, a low magnitude in Figs. 11 and 12 at higher frequencies is desired for appropriate rejection. On the other hand, stator voltage perturbations occur mainly due to: (1) DC voltage bus oscillations at around six times the mains frequency (*i.e.,* 6×60 Hz) and (2) inverter perturbations which are mainly due to harmonic distortion and the switching frequency. These can affect almost all the frequency range, particularly around the synchronous frequency and its harmonics. Therefore, for adequate stator voltage perturbation rejection, a low magnitude in Figs. 11 and 12 in all the frequency range is desired.

From Figs. 11 and 12 it is possible to observe that the responses to sensor noise follow the typical behavior of the complementary sensitivity. In the unperturbed case, all schemes have a very similar response to sensor noise for e_{ds} and $e_{\alpha s}$, whereas for e_{qs} and $e_{\beta s}$ the PI with decoupling networks has a slight amplification around 3000 rad/s. Recalling that the complementary sensitivity is also equal to the resulting closed-loop response, this also indicates that the overall bandwidth is similar for all control schemes. Conversely, when parametric perturbations are considered, the response to sensor noise decreases for the synchronous schemes—particularly for the synchronous PI. However, this also indicates that the bandwidth of the synchronous schemes decreases when perturbed. This is in line with the observation made in the last section: decoupling is reduced for synchronous schemes under this condition. In addition, in the perturbed case a pair of undamped resonance peaks around 300–400 rad/s can be observed in e_{ds} when using the synchronous PI with decoupling networks. These peaks evidence the detuning of the FOC scheme.
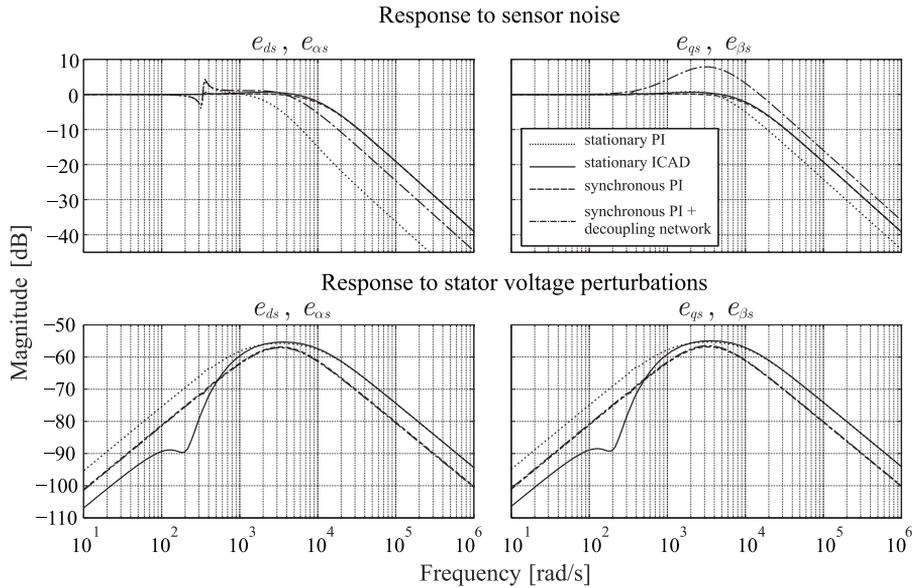
Fig. 12. System response due to perturbations in the stator voltages and sensor noise with parametric perturbations to the rotor time constant and mutual inductance ($\sigma_r = 1.6$ and $\sigma_L = 0.5$).

When no parametric variations are considered, the responses to input perturbations for synchronous frame schemes exhibit the highest perturbation rejection, while the stationary PI scheme has the worst performance—particularly for lower frequencies. If parametric perturbations to the rotor time constant and the mutual inductance are considered, the results are very similar for lower frequencies, but at higher frequencies the stationary frame control schemes have a slight decrease in perturbation rejection.

It can be concluded from the previous analysis that sensor noise must be limited to frequencies higher than the closed-loop bandwidth for all control schemes. In general, all schemes have a similar level of sensibility to sensor noise. This can be elucidated either from the complementary sensitivity analysis shown in this section or with the approach presented in Section 8.1. On the other hand, all control schemes, regardless of the reference frame employed, are sensible to input disturbances mostly around the bandwidth frequency but have a high level of input disturbance rejection at lower and higher frequencies. This indicates that the noise, non-linearities and distortions introduced by the inverter must avoid the stator currents bandwidth, which is typically done by increasing the inverter switching frequency. In general, the synchronous schemes have a slightly better level of input perturbation rejection, particularly when parametric perturbations are considered.

8. Closed-loop stability and the effect of controller bandwidth

In this section a discussion on the effects that the controller bandwidth has on the resulting cross-coupling will be presented. This analysis is complemented by a brief assessment of the resulting stability and robustness margins for all control strategies.

8.1. Effect of controller bandwidth

It has been experimentally observed that the controller bandwidth has a direct influence on the resulting cross-coupling [2,3]. The analysis tools developed in the previous sections allow a measurement of the actual effect of this dynamical characteristic. The controller bandwidth is limited by the inverter switching frequency, with higher frequencies implying additional costs. Therefore, a tool that allows the quantification of the resulting cross-coupling can be a valuable asset when defining the control system specifications.

In the case of the stationary frame current controllers, the system bandwidth can be easily determined with the aid of the Bode plot of the individual channel $c_{1,\text{st}}(s)$, which is the open-loop equivalent of $p_{11,\text{st}}(s)$. In other words, $p_{11,\text{st}}(s)$ is the closed-loop response of $i_{\alpha s}$ with respect to $i_{\alpha s,\text{ref}}$ as defined by (20). Given that $p_{11,\text{st}}(s) = c_{1,\text{st}}(s) \cdot (1 + c_{1,\text{st}}(s))^{-1}$, an algebraic exercise shows that the $c_{1,\text{st}}(s)$ can be expressed in terms of $p_{11,\text{st}}(s)$ as

$$c_{1,\text{st}}(s) = \frac{p_{11,\text{st}}(s)}{1 - p_{11,\text{st}}(s)}. \tag{53}$$

Since the system is symmetrical, the individual channel corresponding to $p_{22,\text{st}}(s)$ is equal to that of $p_{11,\text{st}}(s)$. In other words, $c_{2,\text{st}}(s)$ is similar to $c_{1,\text{st}}(s)$ because the open-loop response of the stator currents is equal for both phases, as are the controllers [25]. For the stationary PI controller the same approach can be used to obtain the individual channels.

The bandwidth of the system employing a synchronous PI controller without and with decoupling networks can be studied through, respectively,

$$c_{i,\text{syn}}(s) = \frac{p_{ii,\text{syn}}(s)}{1 - p_{ii,\text{syn}}(s)}, \quad c_{i,\text{dec}}(s) = \frac{p_{ii,\text{dec}}(s)}{1 - p_{ii,\text{dec}}(s)}. \tag{54}$$

with $i = 1, 2$. However, for the synchronous controllers the symmetry of the individual channels is not preserved; that is, $c_{1,\text{syn}}(s) \neq c_{2,\text{syn}}(s)$. As a result, each channel needs to be analyzed separately.

Fig. 13 shows the Bode plots of $c_{1,\text{st}}(s) = c_{2,\text{st}}(s)$, $c_{1,\text{syn}}(s)$, $c_{1,\text{dec}}(s)$, $c_{2,\text{syn}}(s)$ and $c_{2,\text{dec}}(s)$. According to this figure, the system bandwidth with stationary frame controllers is 5600 rad/s in both cases. For the synchronous PI controller a bandwidth of 5600 and 6500 rad/s is achieved by $c_{1,\text{syn}}(s)$ and $c_{2,\text{syn}}(s)$, respectively. In the case of the synchronous PI controller with decoupling networks it can be observed that individual channels $c_{1,\text{dec}}(s)$ and $c_{2,\text{dec}}(s)$ achieve bandwidths of 6200 and 10100 rad/s, respectively. This shows that the decoupling networks effectively increase the bandwidth of stator current i_{qs}, which is associated with torque production. It should be highlighted that the physical interpretation of the bandwidths of the stationary controllers is not the same as that of their synchronous counterparts because of the difference in the reference frames. However, this information can be used to clarify the requirements for the actuator switching frequency.

To highlight the effects of controller bandwidth the following stationary frame PI and ICAD controllers are considered:

$$k_{1,\text{stPI}}(s) = k_{2,\text{stPI}}(s) = \frac{1040(s + 1000)}{s},$$

$$k_{1,\text{stICAD}}(s) = k_{2,\text{stICAD}}(s) = \frac{1040(s + 1000)}{s} \cdot \frac{(s + 400)^2}{s^2 + 100s + 42500}. \tag{55}$$

As it can be observed, these controllers have the same structure as (16) and (17) with an increased dc gain. In the case of the synchronous controllers the PI was designed according
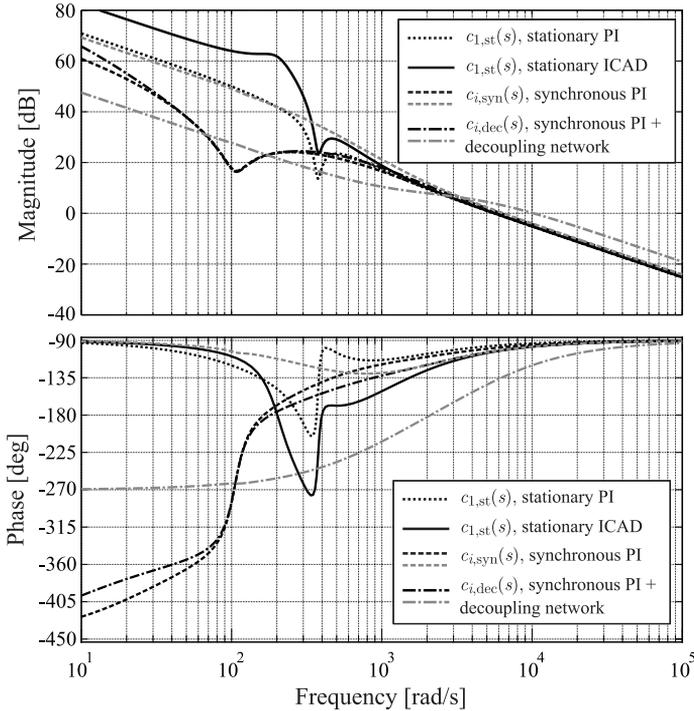
Fig. 13. Equivalent open-loop frequency response of the individual channels. Channel 1 is provided in black and Channel 2 in gray.

Table 2
Maximum cross-coupling magnitude ($\omega_r = 376$ rad/s) with high bandwidth controllers.

Perturbation type	Stationary Frame PI	Stationary Frame ICAD	Synchronous Frame PI	Sync. PI + decoupling
No perturbation	−41 dB	−60 dB	−55 dB	−101 dB
Both perturbations	−54 dB	−72 dB	−46 dB	−76 dB

to (26) and (37) with $a = 5500$, yielding:

$$k_{1,\text{syn}}(s) = k_{2,\text{syn}}(s) = \frac{1093.1(s + 2843)}{s}. \tag{56}$$

The resulting open-loop frequency response with controllers (55) and (56) is presented in Fig. 14. Accordingly, the system bandwidth has increased for all cases.

Figs. 15 and 16 present the closed-loop cross-coupling response for the unperturbed case and when moderate perturbations in mutual inductance and rotor time constant are considered ($\sigma_L = 0.5$ and $\sigma_r = 1.6$). As it can be observed from Fig. 15, an increase of bandwidth results in a reduced closed-loop cross-coupling for all control schemes as expected. Similarly, an increase in bandwidth under the presence of perturbations reflects on a cross-coupling of only −46 dB in the worst case for the synchronous PI controller. The results from this analysis are summarized in Table 2.
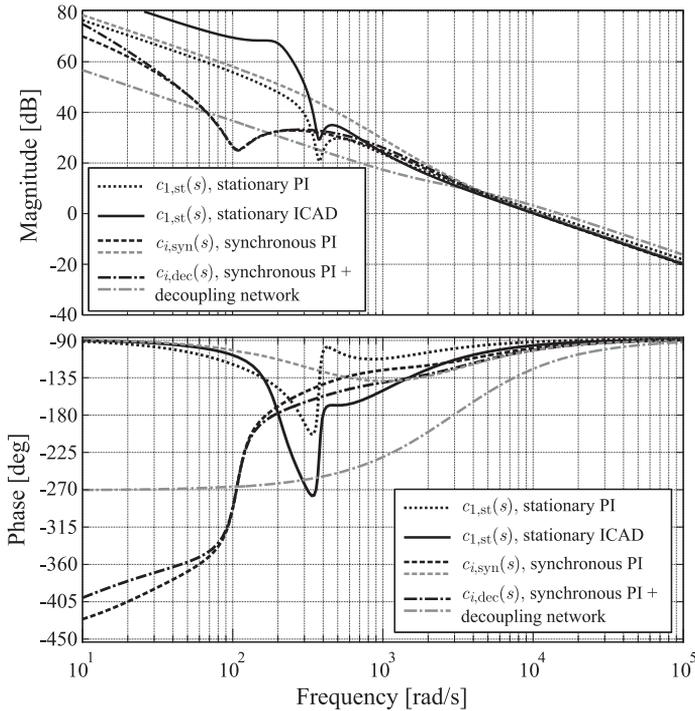
Fig. 14. Equivalent open-loop frequency response of the individual channels using high bandwidth controllers. Channel 1 is provided in black and Channel 2 in gray.
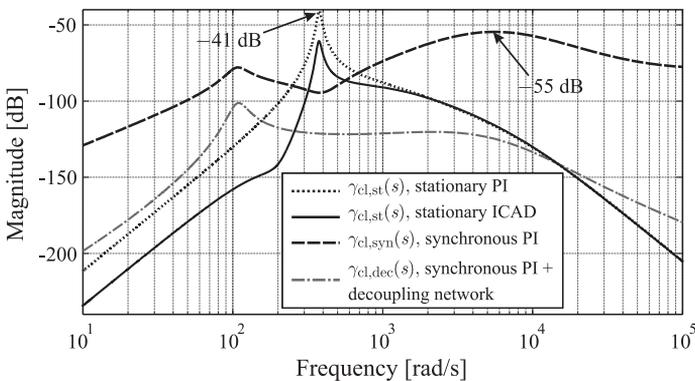
Fig. 15. Unperturbed closed-loop cross-coupling comparison using high bandwidth controllers.

It can be concluded that the closed-loop cross-coupling is effectively reduced by increasing system bandwidth. Although such an increased performance is desirable, care should be exercised as any increment in bandwidth has to be met with an increase of the control system components specifications, such as switching frequency and sensor bandwidth.
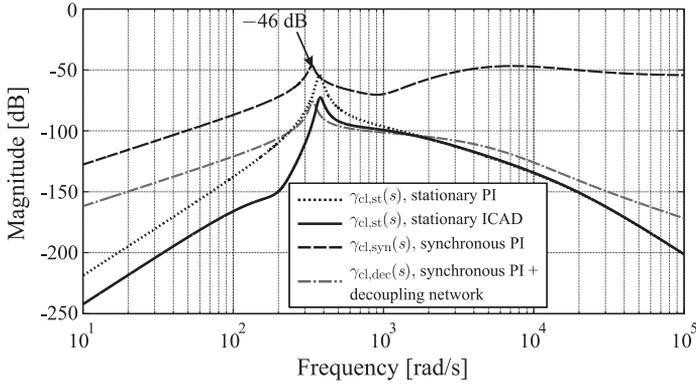
Fig. 16. Closed-loop cross-coupling comparison with perturbations to the rotor time constant and mutual inductance ($\sigma_r = 1.6$ and $\sigma_L = 0.5$) using high bandwidth controllers.

Table 3
Robustness margins ($\omega_r = 376$ rad/s, P_M: phase margin, G_M: gain margin).

Robustness margin		Stationary Frame PI	Stationary Frame ICAD	Synchronous Frame PI	Sync. PI + decoupling
Low Bandwidth	$c_1(s)\ P_M$	83°	76°	81°	78°
	$c_1(s)\ G_M$	15 dB	26 dB	23 dB	23 dB
	$c_2(s)\ P_M$	83°	76°	78°	61°
	$c_2(s)\ G_M$	15 dB	26 dB	∞ dB	7.7 dB
High Bandwidth	$c_1(s)\ P_M$	86°	83°	79°	78°
	$c_1(s)\ G_M$	21 dB	31 dB	31 dB	32 dB
	$c_2(s)\ P_M$	86°	83°	77°	68°
	$c_2(s)\ G_M$	21 dB	31 dB	∞ dB	11 dB

8.2. Closed-loop stability and robustness margins

The analysis presented in the last section can be also used to study the stability and the robustness of the control schemes. As discussed in Section 3, from ICAD theory it is known that the stability of the complete MIMO closed-loop system can be determined by the stability of the SISO individual channels in closed-loop. This allows assessing the robustness of the complete control scheme with the phase and gain margins of the individual channels [19]. These margins are easily determined from the Bode plots of the individual channels presented in the last section (see Figs. 13 and 14) and are summarized in Table 3.

Table 3 shows that in all cases the phase margins are adequate (*i.e.,* greater than 45°), while the gain margins vary from excellent to borderline (*i.e.,* greater than 8 dB) –particularly for individual channel $c_2(s)$ when the synchronous PI with decoupling networks scheme is employed at low bandwidth. Individual channel $c_2(s)$ is associated with stator current i_{qs}, which was also found to exhibit a greater bandwidth for the synchronous PI with decoupling networks schemes in the last section. This clearly shows the trade-off between performance and robustness introduced by the decoupling networks in the torque producing current i_{qs}. A similar trend can be observed in the phase margin of $c_2(s)$; however, in this case the phase margin remains considerably high (61°).
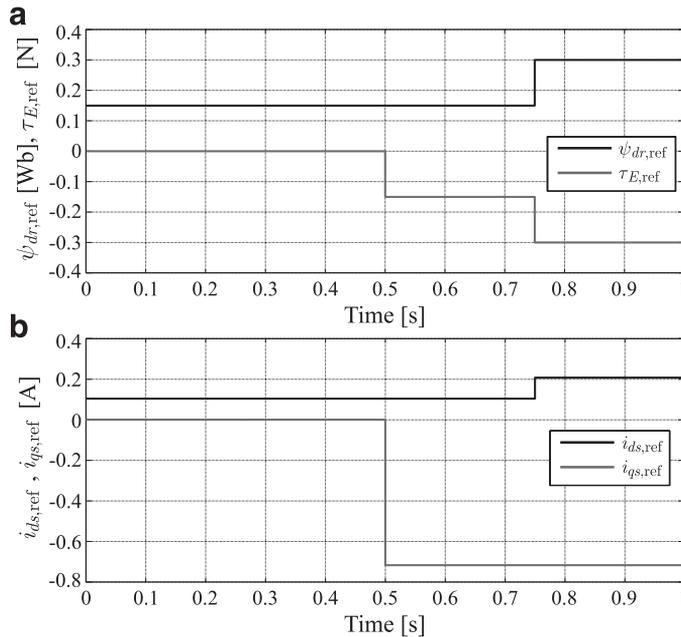
Fig. 17. References used in simulations: (*a*) flux and torque; (*b*) equivalent stator currents.

Except for $c_2(s)$ when the synchronous PI with decoupling networks scheme is employed, the robustness margins of all schemes exhibit marginal differences. Another interesting observation is that robustness is improved in all cases by increasing the bandwidth. However, this should be interpreted carefully because in an experimental setup the possibility of increasing the bandwidth does not only depend on the control algorithm; it also requires adequate sensors, inverter and data processing power—elements which are beyond the analysis presented here.

9. Time-domain simulations

Simulations adopting a common configuration for high-performance applications are carried out to offer further insight into the results from the previous sections. In addition, the effect of the power inverter, which is difficult to determine analytically, is also investigated. The simulations comprise: an IM modeled by (1)–(2); a two-level voltage source inverter (VSI) with a dc bus of 310 V [2]; space vector modulation (SVM) [1]; an approximation of the inverter switching dynamics by a 2nd order system with a time response of 3 μs plus a delay of one switching period; an inverter switching frequency of 10 kHz; and an initial condition of $\omega_r = 376$ rad/s.

References for flux and torque are provided in Fig. 17(*a*). The initial value of the flux is associated to the nominal operating condition of the machine. The flux transients at the beginning of the simulation take approximately 0.5 s and are related to IM initialization. This transient behavior is followed by a change in the torque reference $T_{E,\mathrm{ref}}$ which will induce a change in $i_{qs,\mathrm{ref}}$. Finally, a simultaneous change in the flux and torque references induces a change on $i_{ds,\mathrm{ref}}$ at 0.75 s.

The equivalent current references in the synchronous frame, given by Eq. (33) and obtained using Eq. (24), are shown in Fig. 17(*b*). These can be used to measure the cross-coupling
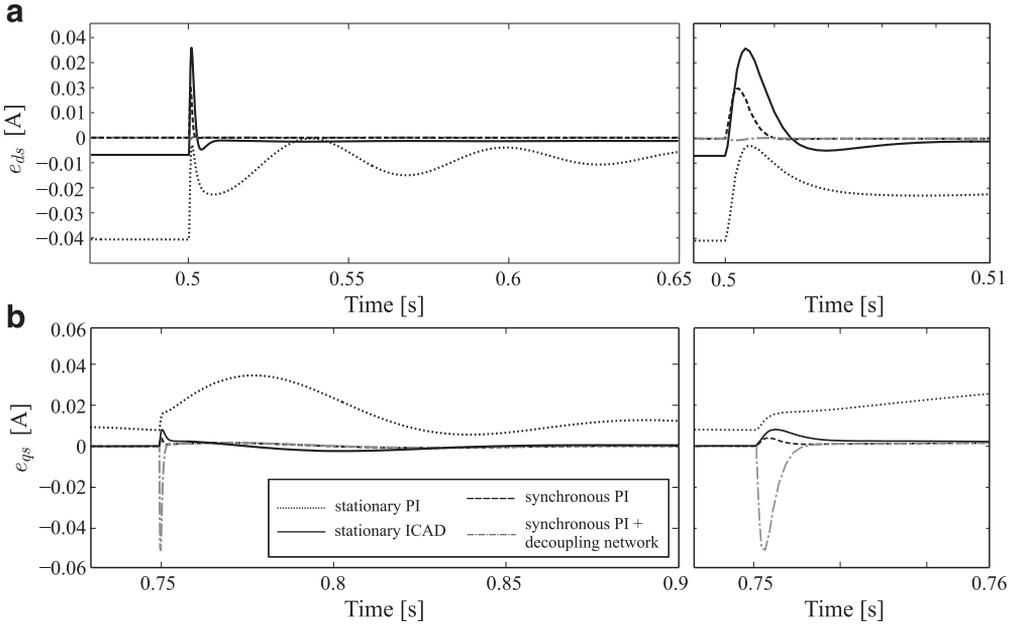
Fig. 18. Error in stator current due to cross-coupling: (a) e_{ds}; (b) e_{qs}.

between the individual channels of i_{ds} and i_{qs} in the time-domain. The error due to cross-coupling is given by $e_{ds} = i_{ds,\mathrm{ref}} - i_{ds}$ around $t = 0.5$ s and $e_{qs} = i_{qs,\mathrm{ref}} - i_{qs}$ around $t = 0.75$ s.

Fig. 18 shows the cross-coupling responses for the different control schemes without considering the inverter dynamics. The current references provided by Fig. 17(b) are used. Given that $i_{ds,\ \mathrm{ref}}$ changes at $t = 0.75$ s, the relevant error due to cross-coupling in the q-axis channel is quantified by e_{qs} and shown around the time of the reference change in Fig. 18. Similarly, as $i_{qs,\ \mathrm{ref}}$ changes at $t = 0.5$ s, it is desirable to assess the effect this has on the d-axis channel at the time of the reference change, which is quantified by e_{ds}. It can be observed that the error in the stationary frame configurations is larger than what Table 1 would indicate. This occurs since in stationary frame control a change in either i_{ds} or in i_{qs} is equivalent to changes in both $i_{\alpha s}$ and $i_{\beta s}$; i.e., the effect of cross-coupling is doubled. In addition, a constant change in a synchronous frame induces an oscillating reference in the stationary frame; also the frequency response of the cross-coupling tends to be greater for ac than for dc. Although the stationary frame controllers are not capable of eliminating the steady-state error as expected, in the case of the ICAD controller it is considerably low when compared with the stationary frame PI. This is mainly due to the increased open-loop gain of the ICAD controller.

On the other hand, it is interesting to see that when decoupling networks are employed a much greater coupling for the i_{qs} current component appears. This happens as in the back-emf compensation (41) it is assumed that $\psi_{dr} = \psi_{\mathrm{ref}}$ and $\psi_{qr} = 0$, which are only satisfied when the FOC controller is properly tuned and the flux reference is constant. In this case Fig. 17(a) shows that precisely at $t = 0.75$ s a flux reference change was simulated. This is in line with the fact that intuitively the decoupling network is greatly dependent on the accurate knowledge of the flux. Nonetheless, the cross-coupling, as measured by the MSF, is still low because a single coupled channel (magnitude of the MSF equal to zero)
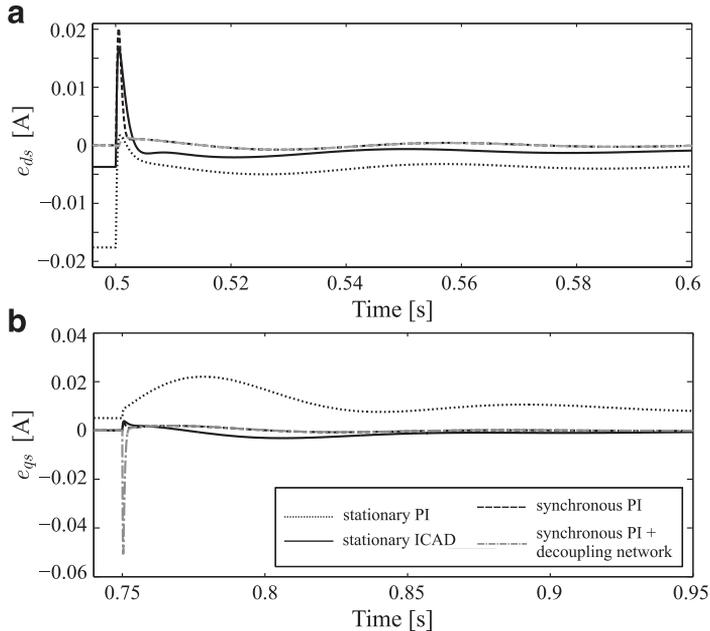
Fig. 19. Error in stator current due to cross-coupling considering perturbations: (*a*) e_{ds}; (*b*) e_{qs}.

does not introduce additional coupling in the closed-loop system; that is, both channels must be coupled for the magnitude of MSF to be greater than zero and, in turn, for the cross-coupling to be problematic for the outer control loop stability [27].

A mild level of parametric perturbation on the mutual inductance and the rotor time constant is considered ($\sigma_L = 0.5$, $\sigma_r = 1.6$), with results shown in Fig. 19. The theoretical results of the last sections indicate that the synchronous frame controller should present an increased cross-coupling while the stationary frame controllers should have decreased cross-coupling. The results from the digital simulations show that these predictions are accurate: the stationary frame controllers exhibit a considerable maximum peak reduction for both i_{ds} and i_{qs}. Conversely the maximum peak for synchronous frame controllers remains mostly unchanged. However, all control schemes present additional frequency components not present in the unperturbed case –particularly for i_{ds}. This indicates that the additional cross-coupling for synchronous frame controllers reflects as oscillatory dynamics as predicted by the MSF analysis. It is difficult to evaluate the actual effect of these dynamics in time-domain; however, the MSF (see Fig. 10) indicates that for the synchronous PI the cross-coupling renders the system more sensible at around 376 rad/s.

Simulations have also been carried out to address the effect of the VSI dynamics on the cross-coupling responses. Results for the unperturbed case are shown in Fig. 20. Overall, the level of the coupling increases due to the added effects of the inverter dynamics. Conversely, results for the perturbed case while including the VSI are presented in Fig. 21. For this last simulation only the initial transient response is shown for the sake of clarity. Although this restriction does not allow presenting the low frequency oscillations found in Fig. 19, these are also present. By comparing Figs. 20 and 21 it is clear that the stationary frame controllers have an important cross-coupling decrement as predicted. Nonetheless, while Fig. 19 indicates
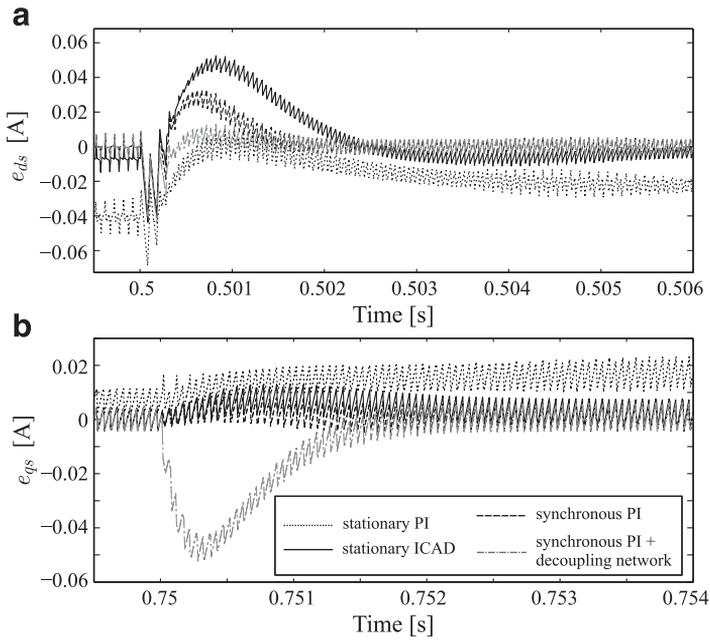
Fig. 20. Error in stator current due to cross-coupling considering inverter dynamics: (*a*) e_{ds}; (*b*) e_{qs}.
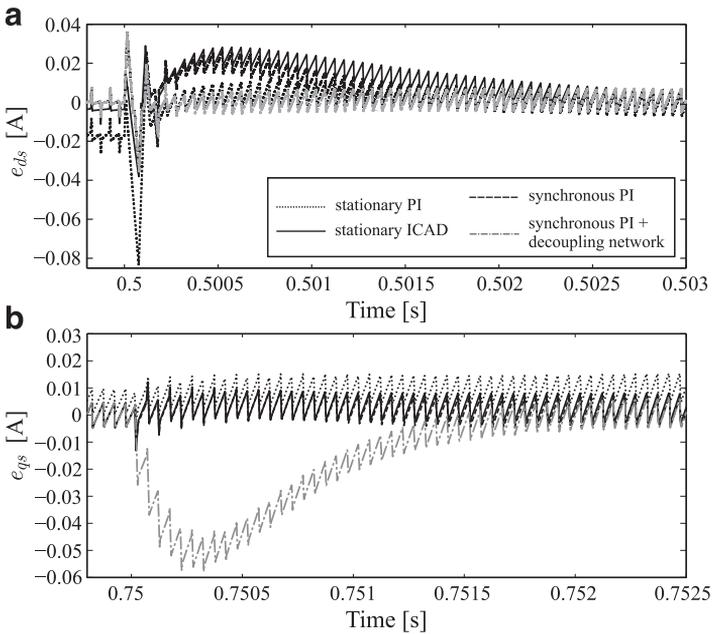
Fig. 21. Error in stator current due to cross-coupling considering inverter dynamics and perturbations: (*a*) e_{ds}; (*b*) e_{qs}.
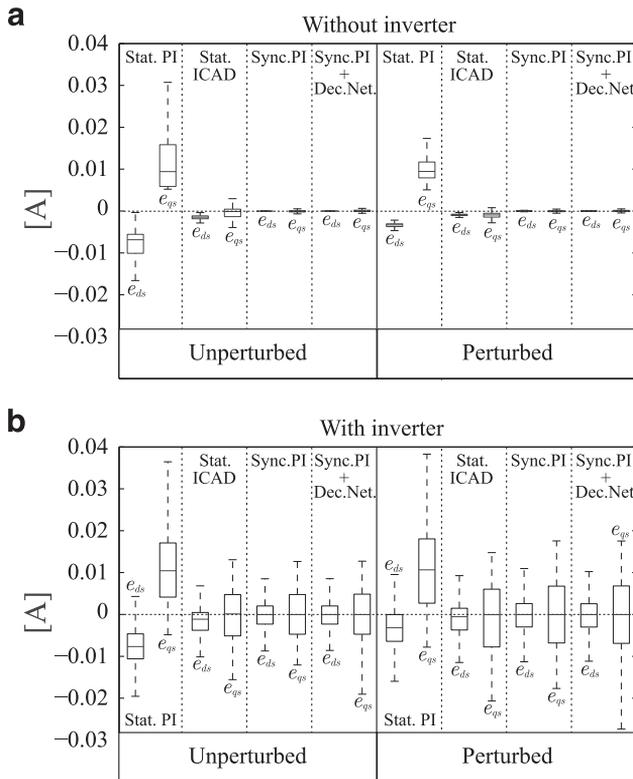
Fig. 22. Box plot of the error in stator current due to cross-coupling: (*a*) when inverter dynamics are neglected; and (*b*) when inverter dynamics are considered.

that the stationary ICAD control scheme has a lower maximum peak cross-coupling than the synchronous PI controller for i_{ds}, the inverter seems to slightly increase the cross-coupling. This could be explained by the increased sensitivity of the stationary frame schemes to perturbations in the stator voltages when parametric perturbations are considered (see Fig. 12). This seems to render these schemes slightly more sensible to the inverter distortions.

In general, if the inverter dynamics are considered a slightly increased cross-coupling results for all conditions and control schemes considered. In particular, results suggest that stationary frame controllers are slightly more sensible to the inverter dynamics—confirming the observations of Section 7. It should be emphasized that simulation results clearly agree with the theoretical predictions of the previous sections even in the presence of the inverter.

9.1. Statistical analysis

To provide a quantitative counterpart to the observations made on the simulation results, a statistical analysis of the resulting cross-coupling error responses is here presented. Fig. 22 shows the *box plot* of errors e_{ds} and e_{qs} for the time ranges $t \in [0.5 \ 0.75]$ and $t \in [0.75 \ 1]$. The analysis is carried out when the inverter dynamics and parametric perturbations are considered and for the case when these are neglected.
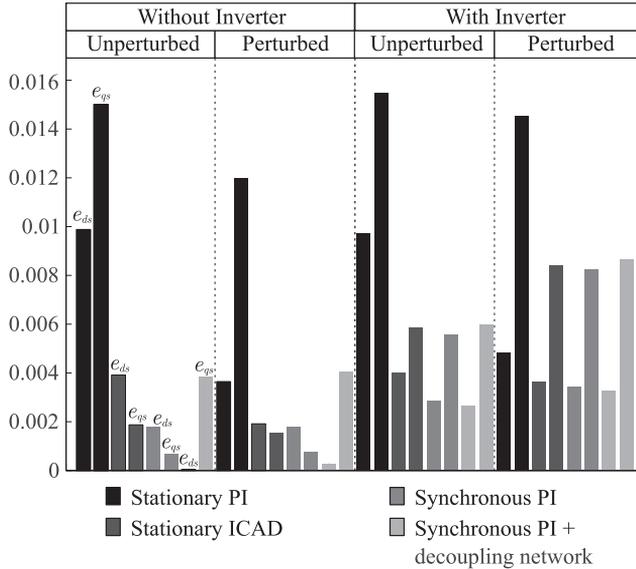
Fig. 23. RMS error of stator currents for several operating conditions due to cross-coupling.

Fig. 22(*a*) shows that the median of the error and the error dispersion (*i.e.*, the length of the quartiles given by the boxes and whiskers of the box plot) for the synchronous frame schemes are much lower than for stationary frame controllers when the inverter is not considered. However, the ICAD stationary controller achieves a significantly lower median and dispersion than the typical stationary frame PI. As predicted by the theoretical results, parametric perturbations actually reduce the error level of the stationary frame schemes.

When the inverter dynamics are considered, the median of the error and error dispersion are increased for all control schemes, as shown by Fig. 22(*b*). A very interesting observation can be made: while the median of the error level is still lower for the synchronous frame schemes, the ICAD controller achieves a similar level of error dispersion than that of synchronous frame schemes. For instance, the dispersion of e_{ds} for the ICAD controller is very similar to that of both synchronous schemes, while the dispersion of e_{qs} for the ICAD controller is actually lower than that of the synchronous frame PI with decoupling networks when parametric perturbations are considered. In all cases the stationary PI has the highest level of median error and dispersion.

The root-mean-square (RMS) error for e_{ds} and e_{qs} for all control schemes is presented in Fig. 23. The RMS error provides further insight as it tends to more significantly penalize the effect of a high error level. This enables a better comparison of the *overall* error level than the median of the error shown in the box plot. When no inverter is considered, Fig. 23 clearly shows that the stationary frame PI has a much higher error level. On the other hand, the synchronous PI controller has a similar level for both e_{ds} and e_{qs}. It is interesting to observe that the synchronous PI with decoupling networks achieves a very low level for e_{ds}; however, the resulting level for e_{qs} is much higher. This is in line with an observation made previously: the effective use of decoupling networks and a synchronous PI is highly dependent on the proper knowledge of the flux level.

The resulting RMS errors for all control schemes increase when the inverter dynamics are considered. For the stationary frame PI, such increment is not significant since the error level was already high compared to the amplitude of the oscillations introduced by the inverter. Conversely, the increment is notable for the other schemes (which incidentally had achieved lower error levels when the inverter was omitted). A particularly important observation is that the introduction of the inverter dynamics renders an almost similar RMS error for both synchronous frame PI schemes regardless of the use of decoupling networks. In addition, the RMS error for the stationary ICAD controller is similar to those of the synchronous schemes. This is a relevant result as it indicates that even when the best level of decoupling is achieved using synchronous frame schemes with decoupling networks, it is also possible for a stationary frame scheme to deliver a comparatively low coupling when other sources of perturbation are accounted for. In other words, *the benefits of reducing the coupling of stator currents are lost to other relevant phenomena such as the inverter distortion once a sufficiently low level of coupling has been achieved*.

10. Conclusion

A framework for assessing the decoupling performance of stator current controllers for IMs has been presented. Using this framework, the cross-coupling characteristics of stationary frame PI control, improved diagonal stationary frame control, synchronous PI control and synchronous PI control with decoupling networks have been evaluated. The methodology includes a procedure for quantifying and analyzing the effect of parametric perturbations in the control system. The studies are based on ICAD's MSF, a frequency valued function fundamental for evaluating the cross-coupling characteristics of multivariable systems. The study carried out in this paper uses full IM models to avoid over-simplifications commonly found in the existing literature. This allows including operating conditions such as the nominal flux and torque into the study.

Findings reveal that the use of a synchronous PI scheme with decoupling networks achieves the best decoupling and robustness to parametric perturbations in all cases. The major disadvantages of this configuration are its complexity and decreased time-domain performance when the flux reference changes. It was found that the synchronous PI scheme is particularly sensible to simultaneous perturbations of the mutual inductance and the rotor time constant. In this condition, cross-coupling is increased around specific frequencies, but the time-domain maximum peak remains similar to the unperturbed case. Conversely, results show that the stationary frame controllers have the greatest cross-coupling of all schemes, particularly stationary frame PI control (*i.e.*, it achieves the lowest decoupling performance). However, stationary frame strategies have the advantages of being simpler to implement and of having a lower sensitivity to parametric perturbations. In addition, stationary frame control can be improved by introducing slightly more complex controllers than a traditional PI control—but still remaining low order and diagonal. It is remarkable that even in the most perturbed scenario the improved diagonal stationary frame control is capable of achieving a decoupling performance similar to that of a synchronous PI scheme.

The effect of the controller bandwidth, sensor noise, stator voltage perturbations and the inverter dynamics over cross-coupling and parametric robustness were also evaluated. Results indicate that an increase in bandwidth effectively decreases cross-coupling and increases robustness for all control schemes. On the other hand, the inverter tends to introduce a slight increment in cross-coupling. This effect seems to be marginally higher for the case

of a stationary frame controller. All schemes present a similar level of sensitivity to sensor noise and rejection of stator voltage perturbations. The study has been complemented with a statistical analysis of the time-domain responses of all control schemes, confirming the theoretical findings.

An important conclusion is that all control schemes are capable of achieving sufficiently low cross-coupling (*i.e.*, sufficiently good decoupling performance) when a similar bandwidth is used; although the stationary frame PI control is remarkably inferior to the others. A synchronous PI with an addition of decoupling networks offers the lowest level of cross-coupling. However, the analyses presented in this article suggest that any further decoupling than that achieved by a standalone synchronous PI scheme or a well-designed stationary frame controller may not be necessary as it only leads to mild advantages for the outer flux-torque control loop.

Appendix A. IM parameters

An identification of the state-space representation of the three-phase DeLorenzo squirrel-cage IM model DL10115A1 has been carried out as in [42]. Using this data the equivalent IM parameters are given as: $R_s = 16.2\ \Omega$, $R_r = 23\ \Omega$, $L_s = 1.44$ H, $L_r = 1.49$ H, $L_m = 1.41$ H and $P = 2$.

References

[1] R. Krishnan, Electric Motor Drives, Prentice Hall, USA, 2001.
[2] J. Chiasson, Modeling and High-Performance Control of Electric Machines, John Wiley & Sons Ltd, Chichester, UK, 2005.
[3] B. Wu, High-power Converters and AC Drives, John Wiley & Sons Ltd, New York, USA, 2006.
[4] J. Rodríguez, et al., High-performance control strategies for electrical drives: An experimental assessment, IEEE Trans. Ind. Electron. 59 (2) (2012) 812–820.
[5] L. Amézquita-Brooks, J. Licéaga-Castro, E. Licéaga-Castro, Speed and position controllers using indirect field-oriented control: a classical control approach, IEEE Trans. Ind. Electron. 61 (4) (2014) 1928–1943.
[6] D.A. Dominic, T.R. Chelliah, Analysis of field-oriented controlled induction motor drives under sensor faults and an overview of sensorless schemes", ISA Trans. 53 (5) (2014) 1680–1694.
[7] M. Hinkkanen, L. Harnefors, J. Luomi, Reduced-order flux observers with stator-resistance adaptation for speed-sensorless induction motor drives, IEEE Trans. Power Electron. 25 (5) (2010) 1173–1183.
[8] D.G. Holmes, B.P. McGrath, S.G. Parker, Current regulation strategies for vector-controlled induction motor drives, IEEE Trans. Ind. Electron. 59 (10) (2012) 3680–3689.
[9] B. Bahrani, S. Kenzelmann, A. Rufer, Multivariable-PI-based dq current control of voltage source converters with superior axis decoupling capability, IEEE Trans. Ind. Electron. 58 (7) (2011) 3016–3026.
[10] D.N. Zmood, D.G. Holmes, Stationary frame current regulation of PWM inverters with zero steady-state error, IEEE Trans. Power Electron. 18 (3) (2003) 814–822.
[11] B. Burton, R.G. Harley, G. Diana, J.L. Rodgerson, Implementation of a neural network to adaptively identify and control VSI-fed induction motor stator currents, IEEE Trans. Ind. Appl. 34 (3) (1998) 580–588.
[12] C. Huang, C. Wei, J. Yu, Y. Hu, Torque and current control of induction motor drives for inverter switching frequency reduction, IEEE Trans. Ind. Electron. 52 (5) (2005) 1364–1371.
[13] J. Lee, J. Hong, K. Nam, R. Ortega, L. Praly, A. Astolfi, Sensorless control of surface-mount permanent-magnet synchronous motors based on a nonlinear observer, IEEE Trans. Power Electron. 25 (2) (2010) 290–297.
[14] R. Vargas, U. Ammann, B. Hudoffsky, J. Rodríguez, P. Wheeler, Predictive torque control of an induction machine fed by a matrix converter with reactive input power control, IEEE Trans. Power Electron. 25 (6) (2010) 1426–1438.
[15] M. Mohseni, S.M. Islam, A new vector-based hysteresis current control scheme for three-phase PWM voltage–source inverters, IEEE Trans. Power Electron. 25 (9) (2010) 2299–2309.

[16] A.K. Abdelsalam, M.I. Masoud, M.S. Hamad, B.W. Williams, Modified indirect vector control technique for current-source induction motor drive, IEEE Trans. Ind. Appl. 48 (6) (2012) 2433–2442.

[17] S.K. Kommuri, J.J. Rath, K.C. Veluvolu, M. Defoort, Y.C. Soh, Decoupled current control and sensor fault detection with second-order sliding mode for induction motor, IET Control Theory Appl. 9 (4) (2015) 608–617.

[18] N. Kumar, T.R. Chelliah, S.P. Srivastava, Adaptive control schemes for improving dynamic performance of efficiency-optimized induction motor drives, ISA Trans. 57 (2015) 301–310.

[19] L.A. Amézquita-Brooks, J. Licéaga-Castro, E. Licéaga-Castro, C.E. Ugalde-Loo, Induction motor control: multivariable analysis and effective decentralized control of stator currents for high-performance applications, IEEE Trans. Ind. Electron. 62 (11) (2015) 6818–6832.

[20] C.E. Ugalde-Loo, L.A. Amézquita-Brooks, E. Licéaga-Castro, J. Licéaga-Castro, Structural robustness assessment of electric machine applications using individual channel analysis and design, Cybern. Phys. 2 (2) (2013) 108–118.

[21] L. Harnefors, H.P. Nee, Model-based current control of AC machines using the internal model control method, IEEE Trans. Ind. Appl. 34 (1) (1998) 133–141.

[22] F. Briz, M.W. Degner, R.D. Lorenz, Analysis and design of current regulators using complex vectors, IEEE Trans. Ind. Appl. 36 (3) (2000) 817–825.

[23] M. Comanescu, L. Xu, T.D. Batzel, Decoupled current control of sensorless induction-motor drives by integral sliding mode, IEEE Trans. Ind. Electron. 55 (11) (2008) 3836–3845.

[24] Y. Liu, J. Zhao, R. Wang, C. Huang, Performance improvement of induction motor current controllers in field-weakening region for electric vehicles, IEEE Trans. Power Electron. 28 (5) (2013) 2468–2482.

[25] L.A. Amézquita-Brooks, E. Licéaga-Castro, J. Licéaga-Castro, Novel design model for the stator currents subsystem of induction motors, Appl. Math. Model. 38 (23) (2014).

[26] J.K. Jain, S. Ghosh, S. Maity, P. Dworak, PI controller design for indirect vector controlled induction motor: a decoupling approach, ISA Trans. 70 (2017) 378–388.

[27] J. O'Reilly, W.E. Leithead, Multivariable control by 'individual channel design', Int. J. Control 54 (1) (1991) 1–46.

[28] S. Skogestad, I. Postlethwaite, Multivariable Feedback Control, John Wiley & Sons Ltd, UK, 2005.

[29] P. Grosdidier, M. Morari, B.R. Holt, Closed-loop properties from steady-state gain information, Ind. Eng. Chem. Fundam. 24 (2) (1985) 221–235.

[30] E. Liceaga-Castro, J. Liceaga-Castro, C.E. Ugalde-Loo, Beyond the existence of diagonal controllers: from the relative gain array to the multivariable structure function, in: Proceedings of the 44th IEEE CDC-ECC, Sevilla, Spain, 2005, pp. 7150–7156.

[31] L.A. Amézquita-Brooks, C.E. Ugalde-Loo, E. Licéaga-Castro, J. Licéaga-Castro, The multivariable structure function as an extension of the RGA matrix: relationship and advantages, Cybern. Phys. 2 (2) (2013) 53–62.

[32] C.E. Ugalde-Loo, E. Acha, E. Licéaga-Castro, Fundamental analysis of the electromechanical oscillation damping control loop of the static VAr compensator using individual channel analysis and design, IEEE Trans. Power Deliv. 25 (4) (2010) 3053–3069.

[33] C.E. Ugalde-Loo, Dynamical modelling of power systems with power electronic controllers using individual channel analysis and design, Phd dissertation, The University of Glasgow, 2009.

[34] C.E. Ugalde-Loo, J.B. Ekanayake, Individual channel analysis of induction generator-based wind turbines, in: Proceedings of the 6th IEEE International Conference on Industrial and Information Systems (ICIIS), Kandy, Sri Lanka, 2011, pp. 1–6.

[35] C.E. Ugalde-Loo, L.A. Amézquita-Brooks, E. Licéaga-Castro, J. Licéaga-Castro, Analysis and efficient control design for generator-side converters of PMSG-based wind and tidal stream turbines, in: Proceedings of the 18th Power Systems Computation Conference (PSCC), Wroclaw, Poland, 2014, pp. 1–7.

[36] J.L. Domínguez-García, C.E. Ugalde-Loo, O. Gomis-Bellmunt, F.D. Bianchi, Input-output signal selection for damping of power system oscillations using wind power plants, Int. J. Electr. Power Energy Syst. 58 (2014) 75–84.

[37] E. Licéaga-Castro, J. Licéaga-Castro, C.E. Ugalde-Loo, E.M. Navarro-López, Efficient multivariable submarine depth-control system design, Ocean Eng. 35 (17–18) (2008) 1747–1758.

[38] J. Licéaga-Castro, C. Ramirez-Espana, E. Licéaga-Castro, GPC control design for a temperature and humidity prototype using ICD analysis, in: Proceedings of the IEEE International CCA, IEEE Conference CACSD, IEEE ISIC, Munich, Germany, 2006, pp. 978–983.

[39] E. Liceaga-Castro, C.E. Ugalde-Loo, J. Liceaga-Castro, P. Ponce, An efficient controller for SV-PWM VSI based on the multivariable structure function, in: Proceedings of the 44th IEEE CDC-ECC, Sevilla, Spain, 2005, pp. 4754–4759.

[40] J. Licéaga, E. Licéaga, L. Amézquita, Multivariable gyroscope control by individual channel design, in: Proceedings of the IEEE International CCA, Toronto, ON, Canada, 2005, pp. 785–790.

[41] W.E. Leithead, J. O'Reilly, Structural issues underlying the performance of 2-input 2-output multivariable systems using individual channel design, in: Proceedings of the 30th IEEE CDC, Brighton, UK, 1991, pp. 575–580.

[42] L. Amézquita-Brooks, J. Licéaga-Castro, E. Licéaga-Castro, Induction motor identification for high performance control design, Int. Rev. Electr. Eng. 4 (5) (2009) 825–836.

[43] L. Amezquita-Brooks, E. Liceaga-Castro, J. Liceaga-Castro, C.E. Ugalde-Loo, Flux-torque cross-coupling analysis of FOC schemes: Novel perturbation rejection characteristics, ISA Trans. 58 (2015) (2015) 446–461.